

## TRACKING DOWN THE SOURCE POPULATION RESPONSIBLE FOR THE UNRESOLVED COSMIC 6–8 KEV BACKGROUND

Y. Q. XUE<sup>1,2,3</sup>, S. X. WANG<sup>1,2</sup>, W. N. BRANDT<sup>1,2</sup>, B. LUO<sup>1,2</sup>, D. M. ALEXANDER<sup>4</sup>, F. E. BAUER<sup>5,6</sup>, A. COMASTRI<sup>7</sup>, A. C. FABIAN<sup>8</sup>, R. GILLI<sup>7</sup>, B. D. LEHMER<sup>9,10</sup>, D. P. SCHNEIDER<sup>1,2</sup>, C. VIGNALI<sup>11</sup>, AND M. YOUNG<sup>1,2</sup>

## ABSTRACT

Using the 4 Ms *Chandra* Deep Field-South (CDF-S) survey, we have identified a sample of 6845 X-ray undetected galaxies that dominates the unresolved  $\approx 20$ –25% of the 6–8 keV cosmic X-ray background (XRB). This sample was constructed by applying mass and color cuts to sources from a parent catalog based on GOODS-South *HST*  $z$ -band imaging of the central 6′-radius area of the 4 Ms CDF-S. The stacked 6–8 keV detection is significant at the  $3.9\sigma$  level, but the stacked emission was not detected in the 4–6 keV band which indicates the existence of an underlying population of highly obscured active galactic nuclei (AGNs). Further examinations of these 6845 galaxies indicate that the galaxies on the top of the blue cloud and with redshifts of  $1 \lesssim z \lesssim 3$ , magnitudes of  $25 \lesssim z_{850} \lesssim 28$ , and stellar masses of  $2 \times 10^8 \lesssim M_*/M_\odot \lesssim 2 \times 10^9$  make the majority contributions to the unresolved 6–8 keV XRB. Such a population is seemingly surprising given that the majority of the X-ray detected AGNs reside in massive ( $\gtrsim 10^{10} M_\odot$ ) galaxies. We discuss constraints upon this underlying AGN population, supporting evidence for relatively low-mass galaxies hosting highly obscured AGNs, and prospects for further boosting the stacked signal.

*Subject headings:* surveys — galaxies: active — diffuse radiation — X-rays: diffuse background — X-rays: galaxies

## 1. INTRODUCTION

Deep extragalactic X-ray surveys have been effective in finding active galactic nuclei (AGNs) out to  $z \approx 5$  (see, e.g., Brandt & Hasinger 2005 and Brandt & Alexander 2010 for reviews), with an observed AGN sky density approaching  $14,900 \text{ deg}^{-2}$  achieved by the deepest X-ray surveys, the *Chandra* Deep Fields (e.g., Brandt et al. 2001; Giacconi et al. 2002; Alexander et al. 2003; Bauer et al. 2004; Luo et al. 2008; Xue et al. 2011, hereafter X11; Lehmer et al. 2012). In both broad (0.5–2 and 2–8 keV) and narrow (0.5–1, 1–2, 2–4, 4–6, and 6–8 keV) energy bands,  $\approx 75$ –95% of the cosmic X-ray background (XRB) emission has been resolved into discrete sources (e.g., Brandt et al. 2000; Mushotzky et al. 2000; Bauer et al. 2004; Worsley et al. 2005; Hickox & Markevitch 2006; Luo et al. 2011), the majority of which are moder-

ately to highly obscured AGNs (e.g., Barger et al. 2003; Szokoly et al. 2004; Tozzi et al. 2006). Of particular interest is the remaining unresolved XRB at the highest energies accessible to *Chandra*, 6–8 keV, since XRB synthesis models (e.g., Gilli et al. 2007) indicate that much of this emission should arise from the highly obscured AGNs that contribute strongly to the XRB near its  $\approx 20$ –40 keV peak.

Recently, utilizing the 4 Ms *Chandra* Deep Field-South (CDF-S; X11) data, Luo et al. (2011) found that the resolved 6–8 keV XRB fraction is  $\approx 78\% \pm 6\%$ , taking into account both the X-ray source contribution and bright-end correction, and adopting the XRB normalization from Hickox & Markevitch (2006; the XRB has a power-law spectral slope of  $\Gamma = 1.4$  and a normalization of  $10.9 \text{ photons s}^{-1} \text{ keV}^{-1} \text{ sr}^{-1}$  at 1 keV).<sup>12</sup> Luo et al. (2011) further found that the unresolved  $\approx 20$ –25% of the XRB in the 6–8 keV band can plausibly be explained by the stacked emission (a  $2.5\sigma$  signal) from a sample of 18,272 X-ray undetected GOODS-South (GOODS-S) *HST*  $z$ -band sources. The above resolved fraction should be considered cautiously as it is known that there is cosmic variance, likely arising from the underlying large-scale structure variations between fields, in the deepest *Chandra* surveys (e.g., Barger et al. 2002, 2003; Cowie et al. 2002; Gilli et al. 2003, 2005; Yang et al. 2003; Hickox & Markevitch 2006; Silverman et al. 2010). The resultant uncertainty in the XRB normalization is likely in the range 10–20% (e.g., Hickox & Markevitch 2006). In this field Luo et al. (2011) obtained the above 6–8 keV stacked signal and it is of interest to understand its origin. Luo et al. (2011) also showed that there should be

<sup>1</sup> Department of Astronomy and Astrophysics, Pennsylvania State University, University Park, PA 16802, USA

<sup>2</sup> Institute for Gravitation and the Cosmos, Pennsylvania State University, University Park, PA 16802, USA

<sup>3</sup> Key Laboratory for Research in Galaxies and Cosmology, Department of Astronomy, University of Science and Technology of China, Chinese Academy of Sciences, Hefei, Anhui 230026, China; xuey@ustc.edu.cn

<sup>4</sup> Department of Physics, Durham University, Durham, DH1 3LE, UK

<sup>5</sup> Pontificia Universidad Católica de Chile, Departamento de Astronomía y Astrofísica, Casilla 306, Santiago 22, Chile

<sup>6</sup> Space Science Institute, 4750 Walnut Street, Suite 205, Boulder, CO 80301, USA

<sup>7</sup> INAF—Osservatorio Astronomico di Bologna, Via Ranzani 1, Bologna, Italy

<sup>8</sup> Institute of Astronomy, Madingley Road, Cambridge, CB3 0HA, UK

<sup>9</sup> The Johns Hopkins University, Homewood Campus, Baltimore, MD 21218, USA

<sup>10</sup> NASA Goddard Space Flight Centre, Code 662, Greenbelt, MD 20771, USA

<sup>11</sup> Università di Bologna, Via Ranzani 1, Bologna, Italy

<sup>12</sup> Throughout this paper, the resolved 6–8 keV XRB fraction refers to the ratio between the detected 6–8 keV surface brightness in the field and the 6–8 keV XRB level determined by Hickox & Markevitch (2006).

an underlying population of highly obscured AGNs hidden among the aforementioned X-ray undetected galaxies. Thanks to superb sensitivities, ultra-deep X-ray observations have already been able to reveal a significant fraction of such previously “missing” highly obscured AGNs (e.g., Alexander et al. 2011; Comastri et al. 2011; Feruglio et al. 2011; Gilli et al. 2011; X11) that are estimated to be roughly as numerous as moderately obscured AGNs (e.g., Gilli et al. 2007).

Mounting evidence has shown that luminous AGNs tend to reside in massive (i.e.,  $M_\star \gtrsim 10^{10} M_\odot$ ;  $M_\star$  is stellar mass) and red galaxies from the local universe up to  $z \approx 3$ –4 (e.g., Barger et al. 2003; Bundy et al. 2008; Brusa et al. 2009; Silverman et al. 2009; Xue et al. 2010, hereafter X10; Mullaney et al. 2012). In this paper, we thus focus on using these mass and color constraints as clues to hunt for an underlying population of highly obscured AGNs responsible for the unresolved  $\approx 20$ –25% of the 6–8 keV XRB. This paper is structured as follows: in § 2 we describe how we estimated physical properties for sources of interest; in § 3 we present the source-stacking analysis and the results obtained; in § 4 we assess the robustness of the stacking results; and in § 5 we discuss the implications of the results.

Throughout, a cosmology of  $H_0 = 70.4 \text{ km s}^{-1} \text{ Mpc}^{-1}$ ,  $\Omega_m = 0.272$ , and  $\Omega_\Lambda = 0.728$  is adopted (e.g., Komatsu et al. 2011). Unless stated otherwise, apparent magnitudes are given in the AB system (Oke & Gunn 1983), and rest-frame absolute magnitudes are given in the Vega system (Johnson & Morgan 1953). We adopt a Galactic column density of  $N_{\text{H}} = 8.8 \times 10^{19} \text{ cm}^{-2}$  (e.g., Stark et al. 1992) along the line of sight to the CDF-S and correct for Galactic extinction in all relevant X-ray analyses below.

## 2. SOURCE PROPERTIES

In this section we describe briefly how we estimated source properties, i.e., redshifts, rest-frame absolute magnitudes, and stellar masses, for sources of interest. The Luo et al. (2011) sample of 18,272 X-ray undetected GOODS-S *HST*  $z$ -band sources is located within  $6'$  of the 4 Ms CDF-S average aim point ( $\alpha_{\text{J2000.0}} = 03^{\text{h}}32^{\text{m}}28.06^{\text{s}}$ ,  $\delta_{\text{J2000.0}} = -27^\circ 48' 26.4''$ ) and outside of twice the 90% encircled-energy (in the 0.5–2 keV band) aperture radius of any 4 Ms CDF-S main-catalog source<sup>13</sup> (the resultant total stacking area is  $0.027 \text{ deg}^2$ ). As shown in Luo et al. (2011), this sample appears to be responsible for the unresolved  $\approx 20$ –25% of the 6–8 keV XRB. Discarding the 160 sources with a low signal-to-noise ratio that were not included in the Dahlen et al. (2010) catalog (detailed below) and the 77 stars that were spectroscopically identified therein (see § 2.3 of Dahlen et al. 2010 for the references of the spectroscopic data used), we reduce the size of the above Luo et al. (2011) sample to 18,035 and refer to this reduced sample as

“Sample A” hereafter. The properties and contribution to the 6–8 keV XRB for Sample A are listed in Table 1, which shows that Sample A still appears to be responsible for the unresolved 6–8 keV signal seen by Luo et al. (2011; see § 3 for the details of the stacking procedure). We provide in Table 2 resolved XRB fractions in various bands between 0.5 and 8 keV for Sample A and additional samples of interest (see § 3). We also directly illustrate the values in Table 2 as Fig. 1.

It can be inferred from Fig. 1 (i.e., the top-most summed data points shown as squares) that there should be a yet-to-be-identified source population that accounts for the remaining  $< 6$  keV emission without boosting significantly the 6–8 keV emission. As shown in § 3, this missing source population cannot be associated with individual galaxies, which would otherwise have been stacked already. It is likely that this remaining  $< 6$  keV emission is from groups/clusters (e.g., Cappelluti et al. 2012), whose emission would not be included in our stacking of galaxies and whose spectrum often has a strong thermal cutoff thus contributing emission in the soft band but not much in the hard band. It is also likely that cosmic variance might play some role here (e.g., affecting the shape of the summed spectrum shown in Fig. 1). Given the complexities in determining resolved XRB fractions (e.g., adopting various methodologies and different XRB normalizations), the resolved XRB fractions reported in Table 2 (i.e., summed contributions of X-ray sources and bright-end correction that range from  $\approx 75\%$  to  $80\%$ ) are in general agreement with those from other works. For example, Hickox & Markevitch (2006) found the resolved XRB fractions to be  $77 \pm 3\%$  and  $80 \pm 8\%$  for the 1–2 and 2–8 keV bands, respectively; Lehmer et al. (2012) obtained resolved XRB fractions of  $76 \pm 4\%$ ,  $82 \pm 13\%$ ,  $88 \pm 14\%$ , and  $82 \pm 9\%$  for the 0.5–2, 2–8, 4–8, and 0.5–8 keV bands, respectively.

### 2.1. Redshifts

Sample A has a  $5\sigma$   $z$ -band limiting magnitude of 28.1, much deeper than most of the photometric-redshift catalogs available in this field (e.g., Cardamone et al. 2010; Rafferty et al. 2011), and thus  $\approx 40\%$  of the Sample A sources (most with  $z_{850} > 26$ ) have no photometric-redshift estimates in those catalogs. Recently, Dahlen et al. (2010) derived photometric redshifts ( $z_{\text{phot}}$ 's) for the 32,508 GOODS-S  $z$ -band sources in the entire GOODS-S region, which include all the 18,035 Sample A sources. We chose to re-derive  $z_{\text{phot}}$ 's for these 32,508 sources in order to ensure consistency of our analyses here (i.e., using an optimized comprehensive set of spectral energy distribution templates throughout; see below) and also include the latest CANDELS *HST*/WFC3 photometry.

We used the ultra-deep 12-band photometry and 1382 secure spectroscopic redshifts ( $z_{\text{spec}}$ 's) assembled by Dahlen et al. (2010; see their § 2.3 for how the quality flag for  $z_{\text{spec}}$  was assigned). The 12-band photometry, covering a wavelength range of  $\approx 0.3$ – $8.0 \mu\text{m}$  in the observed frame, consists of the VLT/VIMOS  $U$ -band; *HST*/ACS F435W, F606W, F775W, and F850LP bands; VLT/ISAAC  $J$ ,  $H$ , and  $K_s$  bands; and *Spitzer*/IRAC 3.6, 4.5, 5.8, and  $8.0 \mu\text{m}$  bands. The photometry (includ-

<sup>13</sup> As described in X11, the 4 Ms CDF-S main catalog contains 740 X-ray sources that are detected with WAVEDETECT at a false-positive probability threshold of  $10^{-5}$  in at least one of three X-ray bands (0.5–8 keV, full band; 0.5–2 keV, soft band; and 2–8 keV, hard band) and also satisfy a binomial-probability source-selection criterion of  $P < 0.004$  (i.e., the probability of sources not being real is less than 0.004). The flux limits at an off-axis angle of  $6'$  for the 4 Ms CDF-S are  $\approx 1.2 \times 10^{-16}$ ,  $3.1 \times 10^{-17}$ , and  $2.6 \times 10^{-16} \text{ erg cm}^{-2} \text{ s}^{-1}$  for the full, soft, and hard bands, respectively.

**Table 1**  
Stacked 6–8 keV Properties

Sample (1)	Criteria (2)	$N_{\text{gal}}$ (3)	Median $z$ (4)	Median $M_{\star}$ ( $M_{\odot}$ ) (5)	Median $C_{\text{eff}}$ (6)	Net Counts (7)	S/N ( $\sigma$ ) (8)	Band Ratio (9)	$\Gamma_{\text{eff}}$ (10)	Total Intensity (11)	Resolved Fraction (%) (12)
A	All galaxies within 6' of aim point	18,035	1.10	$2.3 \times 10^8$	-0.53	819±343	2.4	0.44±0.08	1.67±0.16	1.27	26.1±10.9
B	$M_{\star} \geq 2 \times 10^8 M_{\odot}$	9542	1.48	$8.9 \times 10^8$	-0.45	841±250	3.4	0.46±0.07	1.63±0.13	1.32	26.9±8.0
C	$-0.85 < C_{\text{eff}} < 0$	12,290	1.13	$2.6 \times 10^8$	-0.51	799±283	2.8	0.47±0.10	1.62±0.20	1.24	25.4±9.0
D	$M_{\star} \geq 2 \times 10^8 M_{\odot}$ & $-0.85 < C_{\text{eff}} < 0$	6845	1.59	$8.1 \times 10^8$	-0.48	820±212	3.9	0.48±0.08	1.60±0.16	1.28	26.2±6.8

NOTE. — Col. (1): Sample of galaxies used for stacking. Samples B–D are subsets of Sample A. Col. (2): Criteria used to define the stacked sample (see § 3 for the definition of  $C_{\text{eff}}$ ). Col. (3): Number of galaxies in the stacked sample. Col. (4): Median redshift of the stacked sample. Col. (5): Median stellar mass of the stacked sample. Col. (6): Median effective rest-frame color of the stacked sample. Col. (7): Stacked net source counts in the 6–8 keV band, with  $1\sigma$  Gaussian statistical errors. Col. (8): Stacked signal-to-noise ratio in the 6–8 keV band. Col. (9): Stacked band ratio, defined as the ratio between the observed 2–8 keV and 0.5–2 keV count rates. The  $1\sigma$  errors were calculated following the “numerical method” described in §1.7.3 of Lyons (1991). Col. (10): Effective photon index with  $1\sigma$  errors of the stacked sample. Col. (11): Total 6–8 keV intensity (in units of  $10^{-12}$  erg cm $^{-2}$  s $^{-1}$  deg $^{-2}$ ) of the stacked sample. We calculated effective photon indices and fluxes based on band ratios and aperture-corrected count rates using the CXC’s Portable Interactive Multi-Mission Simulator. Col. (12): Resolved fraction of the 6–8 keV XRB from the stacked sample. We adopted the XRB normalization from Hickox & Markevitch (2006); see § 1.

**Table 2**  
Resolved XRB Fractions in Various Bands

Sample (1)	0.5–1 keV Resolved Frac. (%) (2)	1–2 keV Resolved Frac. (%) (3)	2–4 keV Resolved Frac. (%) (4)	4–6 keV Resolved Frac. (%) (5)	6–8 keV Resolved Frac. (%) (6)
A	9.2 ± 0.8	7.6 ± 0.4	5.8 ± 0.9	< 6.0	26.1 ± 10.9
B	7.9 ± 0.6	6.8 ± 0.3	4.8 ± 0.7	< 4.4	26.9 ± 8.0
C	5.7 ± 0.7	5.0 ± 0.3	3.3 ± 0.8	< 4.9	25.4 ± 9.0
D	5.0 ± 0.5	4.6 ± 0.3	3.1 ± 0.6	< 3.7	26.2 ± 6.8
X-ray sources	21.0 ± 5.3	26.5 ± 5.1	38.1 ± 5.2	43.4 ± 5.2	47.7 ± 5.5
Bright-end correction	58.9 ± 4.2	47.8 ± 3.4	38.9 ± 2.7	33.1 ± 2.3	29.8 ± 2.1
X-ray src. + corr. + D	84.8 ± 6.7	78.9 ± 6.1	80.1 ± 5.9	76.5 $^{+6.8}_{-5.7}$	103.7 ± 9.1

Notes. — Col. (1): Samples A, B, C, and D are the same as those in Table 1. The fifth and sixth rows represent XRB fractions resolved by X-ray point sources in the 4 Ms CDF-S and the corresponding bright-end correction (Luo et al. 2011; also see § 1). The last row is the sum of contributions from X-ray point sources, the bright-end correction, and Sample D. Cols. (2–6): Resolved XRB fractions and  $1\sigma$  uncertainties in various bands. In Col. (5), the “<” signs for Samples A, B, C, and D indicate  $3\sigma$  upper limits on resolved fractions in the 4–6 keV band, where the upper limit for Sample D was used to determine the upper error of the total contribution in this band. We adopted the XRB normalization from Hickox & Markevitch (2006); see § 1.

ing upper limits<sup>14</sup>) was obtained using the TFIT algorithm that performs point-spread-function matched photometry uniformly across different instruments and filters (see Dahlen et al. 2010 for details). Additionally, we also included the latest photometry in the *HST*/WFC3 F105W (*Y*), F125W (*J*), and F160W (*H*) bands, based on the first 10-epoch GOODS-S images from CANDELS (Grogin et al. 2011; Koekemoer et al. 2011) that are publicly available. For the CANDELS Deep and Wide regions that have multi-epoch *J* and *H* coverage, the images were stacked for each band in each region using the published weight maps by the CANDELS group. Object catalogs were generated using SExtractor (Bertin & Arnouts 1996) version 2.8.6, and then source matching was performed with the Dahlen et al. (2010) catalog using the SExtractor ASSOC option, searching for the nearest match within 0.5". The *J*-band photometry was done with the SExtractor single-image mode, while the *H*-band photometry was extracted with the dual-image mode to match detections in *J*. The photometry on *Y*-band images was extracted only using the single-image mode because of its different sky coverage from *J* and *H* images. For sources that have *J* and *H* de-

tections in both the *HST*/WFC3 and VLT/ISAAC, we found the two sets of *J* and *H* measurements in reasonable agreement without any apparent systematic offsets; for these sources, we chose to adopt the measurements from *HST*/WFC3 and discard those from VLT/ISAAC because the *HST*/WFC3 photometry is of higher quality. The  $5\sigma$  limiting magnitudes for point sources are the following: 28.0 for the VIMOS *U*-band; 28.7, 28.8, 28.3, and 28.1 for the ACS F435W, F606W, F775W, and F850LP bands; 25.0, 24.5, and 24.4 for the ISAAC *J*, *H*, and *K<sub>s</sub>* bands; 26.1, 25.5, 23.5, and 23.4 for the IRAC 3.6, 4.5, 5.8, and 8.0  $\mu\text{m}$  bands (see § 2.1 of Dahlen et al. 2010 for details); and 28.2, 27.9, and 27.6 for the WFC3 F105W, F125W, and F160W bands (see Table 6 of Grogin et al. 2011 for details), respectively.

Utilizing the Zurich Extragalactic Bayesian Redshift Analyzer (ZEBRA; Feldmann et al. 2006), we adopted a procedure similar to that detailed in Luo et al. (2010) and Rafferty et al. (2011) to calculate  $z_{\text{phot}}$ ’s down to  $z_{850} \approx 28.1$ . As is standard practice, we constructed our galaxy spectral energy distribution (SED) templates based on the stellar population synthesis model by Bruzual & Charlot (2003) with a Chabrier initial-mass function (IMF; Chabrier 2003) and a dust-extinction law from Calzetti et al. (2000). The adopted star-formation history is of exponential form,  $e^{-t/\tau}$ , with  $\log(\tau/\text{year})$  ranging from 6.5 to 11.0 and  $\log(\text{age}/\text{year})$  ranging from 7.0 to 10.1 (both in steps of 0.1). The dust extinction

<sup>14</sup> For photometry reported by TFIT with a negative flux value or a positive flux value that is equal or smaller than its error  $\sigma_f$  (i.e., with a  $\leq 1$  signal-to-noise ratio), we incorporate this information as a flux upper limit (i.e., with coverage but no detection) by setting both the values of flux and its error to be  $\sigma_f$ .

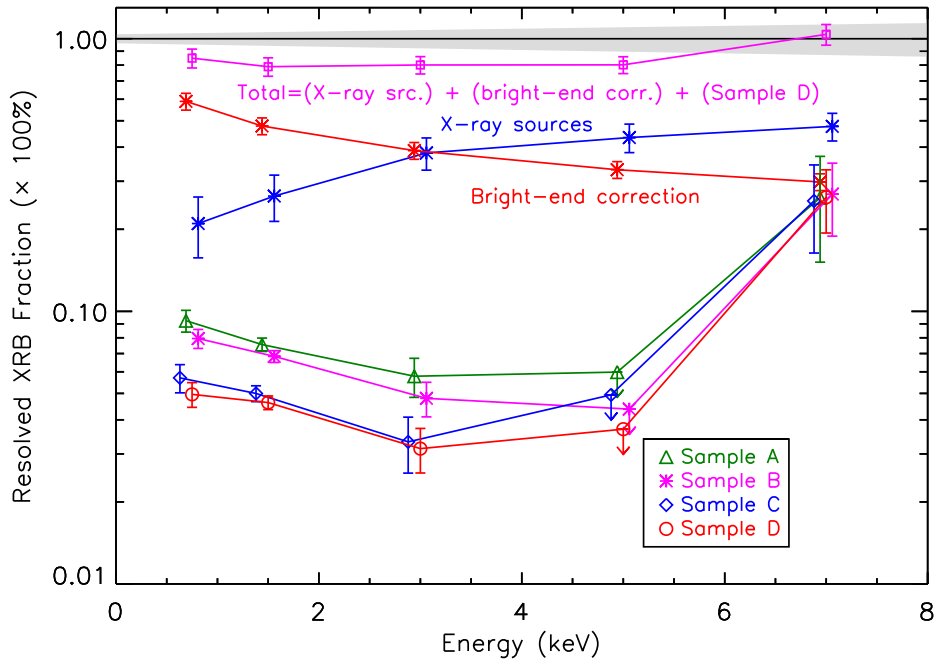


**Figure 1.** Resolved XRB fractions in five energy bands between 0.5 and 8 keV; this figure illustrates the values in Table 2 (details are therefore referred to Table 2; cf. Fig. 6 of Luo et al. 2011). The data points are shifted slightly in the  $x$ -direction for clarity. The total XRB intensities are adopted from Hickox & Markevitch (2006; also see § 1) with uncertainties indicated by the gray area.

$A_V$  varies between 0 and 3.0 (also in steps of 0.1), and the metallicities are  $Z = 0.004, 0.008, 0.02$  (roughly solar), and 0.05. Using the available 1382 secure  $z_{\text{spec}}$ 's (redshifts were fixed to the  $z_{\text{spec}}$  values for training purposes), we first ran ZEBRA to identify and apply systematic offsets in the photometry (differing from filter to filter; typically  $\lesssim 0.3$  mag) that minimized the residuals between observed and best-fit template fluxes. We then used ZEBRA to construct new templates by modifying the original templates based on the best fits between the corrected photometry and original templates. Finally we ran ZEBRA on all 32,508 sources, using the corrected photometry and an improved set of templates, to derive  $z_{\text{phot}}$ 's.

We used the normalized median absolute deviation

$$\sigma_{\text{NMAD}} = 1.48 \times \text{median} \left( \left| \frac{\Delta z - \text{median}(\Delta z)}{1 + z_{\text{spec}}} \right| \right), \quad (1)$$

where  $\Delta z = z_{\text{phot}} - z_{\text{spec}}$ , and the outlier fraction [outliers are defined as sources with  $|\Delta z/(1 + z_{\text{spec}})| > 0.15$ ] to assess the  $z_{\text{phot}}$  quality. For the spectroscopic subsample, we find  $\sigma_{\text{NMAD}} = 0.005$  and an outlier fraction of 1.8%. However, the above evaluation cannot represent the real quality of the  $z_{\text{phot}}$ 's, because the SED templates were modified using the  $z_{\text{spec}}$  information, and we are thus biased to get optimal fitting results for the spectroscopic subsample. Therefore, to obtain a realistic estimate of the  $z_{\text{phot}}$  quality for the sources lacking  $z_{\text{spec}}$ 's (i.e., no training possible), we performed a series of blind tests. We randomly selected 3/4 of the  $z_{\text{spec}}$  sources to go through the above training procedure (i.e., photometry correction and template improvement). We then derived  $z_{\text{phot}}$ 's for the remaining 1/4  $z_{\text{spec}}$  sources (i.e., blind-test sources whose  $z_{\text{spec}}$  information was not

utilized) based on the corrected photometry and the expanded set of templates. The blind test was repeated ten times to ensure a statistically meaningful assessment, which means that there are duplicated blind-test sources because a  $z_{\text{spec}}$  source will on average be used for blind testing 2.5 times. Figure 2 shows the  $z_{\text{phot}}$  quality results from the blind tests. We obtained  $\sigma_{\text{NMAD}} = 0.043$  and an outlier fraction of 7.1% for the blind tests.

We defined  $\sigma_{\text{NMAD}}^+$  and  $\sigma_{\text{NMAD}}^-$  to examine further the  $z_{\text{phot}}$  accuracy as a function of  $z_{850}$  magnitude, where  $\sigma_{\text{NMAD}}^+$  is calculated for sources with  $z_{\text{phot}} > z_{\text{spec}}$  using Eq. 1 and  $\sigma_{\text{NMAD}}^-$  for sources with  $z_{\text{phot}} < z_{\text{spec}}$ . The  $\sigma_{\text{NMAD}}^+$  and  $\sigma_{\text{NMAD}}^-$  running curves are shown in Fig. 2a (red and blue curves), both of which are roughly constant ( $\approx \pm 0.03$ ) and symmetric around the  $\Delta z/(1 + z_{\text{spec}}) = 0$  axis (dashed line) across a wide range of  $z_{850}$  magnitude. Therefore, our  $z_{\text{phot}}$  quality appears to be reasonably accurate and free of strong systematics down to faint magnitudes, as can also be inferred from Figs. 2b–2d that show the histograms of  $\Delta z/(1 + z_{\text{spec}})$  in various intervals of  $z_{850}$  magnitude.

Strictly speaking, the above blind-test analysis of  $z_{\text{phot}}$  quality is really only applicable for  $z_{850} \lesssim 25.2$  mag (the rough limit of the spectroscopic data available), given that some of the bandpasses used in the analysis have dropped toward fainter magnitudes.<sup>15</sup> To explore effectively the true behavior of  $z_{\text{phot}}$  quality at fainter magnitudes, we performed four additional series of blind tests

<sup>15</sup> We examined the mean number of detection bands ( $N_{\text{filter}}$ ) as a function of  $z_{850}$  magnitude for all the 32,508 sources in the Dahlen et al. (2010) catalog (cf. Fig. 8b of Luo et al. 2010). We find that  $N_{\text{filter}}$  is no less than  $\approx 10$  for sources with  $z_{850} < 25$  mag, while  $N_{\text{filter}}$  drops from  $\approx 10$  to  $\approx 7$  as  $z_{850}$  goes from  $\approx 25$  mag to  $\approx 28$  mag.

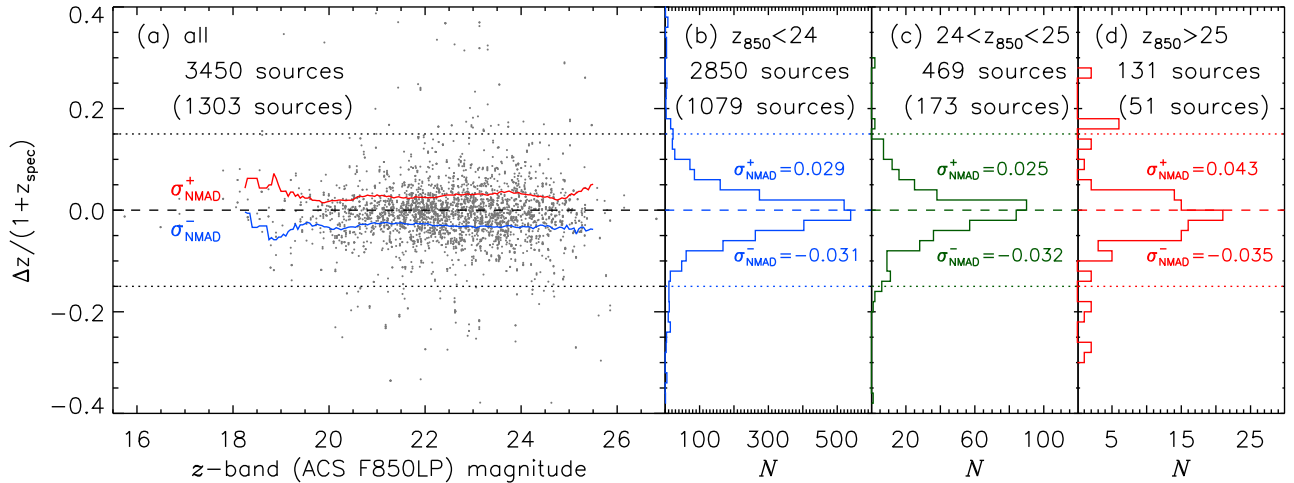


**Figure 2.** Blind-test results of photometric redshifts for all sources with  $z_{\text{spec}}$  (i.e., including duplicate ones). (a)  $\Delta z/(1+z_{\text{spec}})$  as a function of  $z$ -band magnitude. The  $\sigma_{\text{NMAD}}^+$  and  $\sigma_{\text{NMAD}}^-$  running curves (both computed in bins of  $\Delta z_{850} = 1$  mag) are shown as red and blue curves, respectively. (b–d) Histograms of  $\Delta z/(1+z_{\text{spec}})$  in various intervals of  $z_{850}$  magnitude, with corresponding values of  $\sigma_{\text{NMAD}}^+$  and  $\sigma_{\text{NMAD}}^-$  annotated. In each of the four panels (a–d), the number of all sources is shown without parentheses and the number of unique sources (i.e., excluding duplicate ones) is shown in parentheses. The dashed line indicates  $\Delta z/(1+z_{\text{spec}}) = 0$ , and the dotted lines indicate the threshold values of outliers [i.e.,  $\Delta z/(1+z_{\text{spec}}) = \pm 0.15$ ].

(denoted as cases i–iv) that are almost identical to the previous blind tests with the only difference being the utilization of “faked” photometry in four different ways. We faked the photometry of the  $z_{\text{spec}}$  subsample as follows. For each  $z_{\text{spec}}$  source, we first randomly picked a faint (i.e.,  $z_{850} > 25$  mag), non- $z_{\text{spec}}$  source either from the Dahlen et al. (2010) catalog (a total of 32,508 sources) or from Sample D (a total of 6845 sources, whose stacked 6–8 keV emission can account entirely for the unresolved  $\approx 20$ –25% of the 6–8 keV XRB; see § 3 for details). We then applied the band coverage of the randomly picked  $z_{\text{phot}}$  source to the  $z_{\text{spec}}$  source. Specifically, for each filter considered, (1) if the  $z_{\text{phot}}$  source was not observed, we then set the  $z_{\text{spec}}$  source as non-observed; (2) if the  $z_{\text{phot}}$  source was not detected (i.e., upper limits applied), we then either set the  $z_{\text{spec}}$  source as non-observed (this corresponds to the worst scenario where all information was discarded) or set the  $z_{\text{spec}}$  source as non-detected (i.e., we added a random  $1\sigma$  fluctuation to the flux of the  $z_{\text{spec}}$  source to simulate the photometric quality of the  $z_{\text{phot}}$  source and treated the derived flux as an upper limit); and (3) if the  $z_{\text{phot}}$  source was detected, we then did nothing with the photometry of the  $z_{\text{spec}}$  source. The various combinations of parent sample (the Dahlen et al. catalog vs. Sample D) and photometry treatment of the  $z_{\text{spec}}$  source (non-observed vs. non-detected, when the  $z_{\text{phot}}$  source was not detected) lead to cases i–iv. Table 3 shows the  $z_{\text{phot}}$  quality blind-test results for cases i–iv where “faked” photometry was utilized. As an example, Figure 3 shows the results for case iv. Overall, the obtained  $\sigma_{\text{NMAD}}$  ranges from 0.049 to 0.055 (cf.  $\sigma_{\text{NMAD}} = 0.043$  obtained in previous blind tests) and the outlier fraction ranges from 10.4% to 13.1% (cf. an outlier fraction of 7.1% obtained previously). These analyses suggest that in our case the reduction of bandpass coverage at  $z_{850} > 25$  mag does degrade the  $z_{\text{phot}}$  quality to some degree, which is expected, but not severely overall.

We also made different versions of Figs. 2 and 3 using only  $z_{\text{spec}} > 1$  sources. We find that these versions resemble the original Figs. 2 and 3 closely in terms of values

of  $\sigma_{\text{NMAD}}^+/\sigma_{\text{NMAD}}^-$  and outlier fractions. This analysis shows that there is no apparent degradation of our  $z_{\text{phot}}$  quality toward high redshifts.

We then compared our  $z_{\text{phot}}$ ’s with other photometric-redshift catalogs in this and other fields. In general, our  $z_{\text{phot}}$  quality (in terms of  $\sigma_{\text{NMAD}}$  and outlier fraction) is consistent with that of Cardamone et al. (2010), Dahlen et al. (2010), Luo et al. (2010), Rafferty et al. (2011), and Salvato et al. (2011) at similar magnitudes (the first four catalogs have CDF-S coverage while the fifth one is in the COSMOS field). Further source-to-source comparison with any of the four CDF-S catalogs reveals no strong systematic difference in the  $z_{\text{phot}}$ ’s at any magnitudes, and the typical difference in the  $z_{\text{phot}}$  estimates is at the same level as the reported error bars [ $\text{median}(|z_{\text{phot},\text{Xue}} - z_{\text{phot},\text{other}}|) \sim \sigma_{z_{\text{phot}}} \sim 0.15$ ].

Overall 779 out of the 18,035 sources (4.3%) in Sample A have secure  $z_{\text{spec}}$ ’s, while Sample D contains 537 sources (7.8%) with a secure  $z_{\text{spec}}$  out of its total 6845 sources. For Sample D sources, we find acceptable agreement between our  $z_{\text{phot}}$ ’s and those of Dahlen et al. (2010) ( $\sigma_{\text{NMAD}} = 0.080$ ), despite the different methodologies adopted and the challenging nature of deriving  $z_{\text{phot}}$ ’s for these faint sources (see § 3).

## 2.2. Rest-Frame Absolute Magnitudes

We followed the procedure in § 3.1 of X10 to derive rest-frame absolute magnitudes for each Sample A source up to its reddest rest-frame detection band ( $K$ -,  $H$ -,  $J$ -,  $I$ -,  $R$ -,  $V$ -, or  $B$ -band). Briefly, we adopted the approach of template SED fitting, which has the advantage of potentially reducing catastrophic failures in cases of limited/incomplete photometric coverage, as opposed to the approach of linear or log-linear interpolation/extrapolation based on photometric data. With the input of the aforementioned Dahlen et al. (2010; 12-band photometry) and CANDELS ( $Y$ ,  $J$ , and  $H$ ) photometry as well as the improved set of templates (see § 2.1), we utilized ZEBRA to identify the best-fit template for each source by fixing the source redshift to the corresponding

**Table 3**  
 $z_{\text{phot}}$  Blind-Test Results with the Utilization of Faked Photometry

Case	Parent Sample	Photometry Treatment	$\sigma_{\text{NMAD}}$	Outlier Fraction
i	Dahlen et al. catalog	Non-observed	0.055	13.1%
ii	Dahlen et al. catalog	Non-detected	0.053	11.5%
iii	Sample D	Non-observed	0.051	11.3%
iv	Sample D	Non-detected	0.049	10.4%

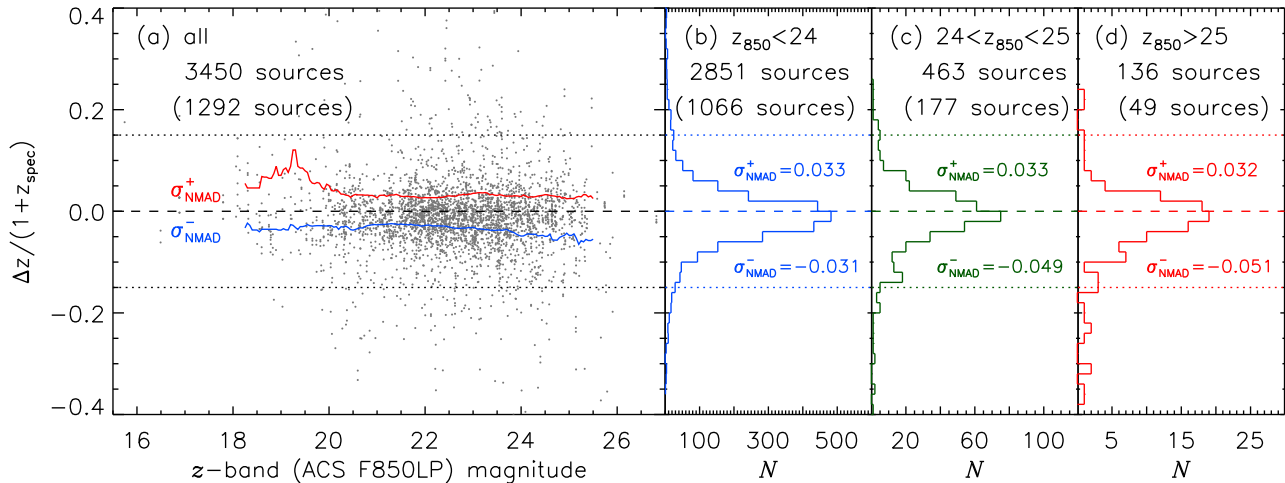


**Figure 3.** Same as Figure 2, but derived with the utilization of faked photometry (corresponding to case iv; see § 2.1).

$z_{\text{spec}}$  (if available) or  $z_{\text{phot}}$ . We then derived rest-frame absolute magnitudes for each source based on the best-fit template. Dust extinction is folded into our galaxy SED templates (see § 2.1), so the derived rest-frame absolute magnitudes are not extinction corrected.

### 2.3. Stellar Masses

We adopted the approach described in § 3.2 of X10 to derive stellar masses ( $M_{\star}$ ) for the Sample A sources. Using the tight correlations between rest-frame optical/near-infrared colors and stellar mass-to-light ratios obtained by Zibetti et al. (2009),

$$\log(M_{\lambda,\star}/M_{\odot}) = \log(L_{\lambda}/L_{\lambda,\odot}) + b_{\lambda}(M_{\text{B}} - M_{\text{V}}) + a_{\lambda} + 0.20, \quad (2)$$

we estimated a set of stellar masses at various rest-frame bands (denoted as  $\lambda$ ) for each source (the values of the coefficients,  $a_{\lambda}$  and  $b_{\lambda}$ , can be found in Table B1 of Zibetti et al. 2009). The above equation was derived by constructing spatially resolved maps of stellar-mass surface density in galaxies, based on the high-quality optical and near-infrared imaging data of a sample of nine nearby galaxies that span a broad range of morphologies and physical properties (Zibetti et al. 2009). When deriving Eq. 2, Zibetti et al. (2009) took into account the effects of dust in their models. Thus,  $L_{\lambda}$  and  $M_{\text{B}} - M_{\text{V}}$  in Eq. 2 are the observed (dust-extincted) luminosity and rest-frame color. A caveat pointed out by Zibetti et al. (2009) is that stellar masses of dusty starburst galaxies estimated using unresolved photometry are likely underestimated by up to 40% because dusty regions are under-represented in the measured fluxes. In Eq. 2 we have adjusted the normalization by 0.20 dex to account for our adopted Salpeter (1955) IMF for stellar-mass esti-

mates.<sup>16</sup> We selected the stellar-mass estimate that corresponds to the actual reddest rest-frame detection band of the source<sup>17</sup> because longer-wavelength (e.g.,  $K$ -band) galaxy luminosities are much less sensitive to dust and stellar-population effects than shorter-wavelength luminosities (e.g., Bell & de Jong 2000).

Using simulations, we assessed the uncertainties associated with stellar-mass estimates that arise from our procedure for deriving photometric redshifts and rest-frame absolute magnitudes based on template SED fitting. For each Sample A source, which has a photometric redshift  $z_{\text{phot},i}$  and an associated 1-sigma error  $\sigma_{\text{phot},i}$ , we randomly drew a value  $z_{\text{sim},i}$  (i.e., the simulated photometric redshift) from the range of  $z_{\text{phot},i} \pm \sigma_{\text{phot},i}$  conservatively assuming a uniform distribution. We then derived the simulated rest-frame absolute magnitudes for the source using  $z_{\text{sim},i}$ , the aforementioned photometry, and the improved set of templates (see § 2.1), following the procedure detailed in § 2.2. Finally, we obtained a simulated stellar-mass estimate for the source using Eq. 2. For Sample A sources, we found no systematic offset between the set of simulated stellar-mass estimates ( $M_{\star,\text{sim}}$ ) and the set of real stellar-mass estimates ( $M_{\star}$ ), i.e., the distribution of the logarithmic ratio between these two sets of stellar-mass estimates [ $R = \log(M_{\star,\text{sim}}/M_{\star})$ ] is symmetric and peaks at zero; furthermore, the scatter of  $R$  is 0.22 dex and largely independent of stellar mass. Given that the photometric-redshift errors derived with

<sup>16</sup> In this paper, we have adopted a conversion factor of  $\approx 0.20$  dex (i.e.,  $\approx 1.6$ ) between stellar masses estimated using a Salpeter IMF and a Chabrier IMF (with the former stellar masses being systematically larger).

<sup>17</sup> Of the Sample A (Sample D) sources, 94.7%, 79.5%, and 57.0% (94.2%, 83.2%, and 59.8%) have rest-frame  $R$ -band,  $J$ -band, and  $K$ -band detections (detection indicates a  $> 1\sigma$  signal; see Footnote 14) or beyond, respectively.



ZEBRA generally underestimate the true errors by a factor of  $\approx 3\text{--}6$  (see, e.g., § 3.4 of Luo et al. 2010), we repeated the above simulation four times by randomly drawing  $z_{\text{sim},i}$  from the range of  $z_{\text{phot},i} \pm n\sigma_{\text{phot},i}$  (where  $n = 3, 4, 5,$  and  $6$ ) assuming a uniform distribution. In these four additional simulations, we also found no systematic offset between  $M_{\star,\text{sim}}$  and  $M_{\star}$  values; the scatter of  $R$  is 0.40, 0.45, 0.50, and 0.56 dex for  $n = 3, 4, 5,$  and  $6$ , respectively. We expect to have smaller scatters in  $R$  if we randomly draw  $z_{\text{sim},i}$  assuming a Gaussian distribution that peaks at  $z_{\text{phot},i}$ , which is likely closer to reality. The above analyses show that the stellar-mass errors produced by the uncertainties of photometric redshifts and rest-frame absolute magnitudes are typically smaller than  $\approx 0.2\text{--}0.5$  dex.

We assessed the robustness of our stellar-mass estimates through several checks. First, we compared our stellar-mass estimates with those presented by X10 and Mullaney et al. (2012). For all sources in X10 and Mullaney et al. (2012), we find general agreement between common sources, with a median ratio of  $\approx 1.0$  between the two estimates (after taking into account different choices of IMFs and rest-frame bands that are used for stellar-mass estimates) and  $\lesssim 0.35$  dex random scatter. Second, we compared our galaxy stellar-mass distributions to those in the COSMOS field. Ilbert et al. (2010) computed the stellar masses of the COSMOS galaxies where sources with  $i^+ < 25.0$  have the most reliable photometric redshifts and mass estimates. For each of the chosen Subaru  $i^+$ -band limiting magnitudes (i.e.,  $i^+_{\text{limit}} = 22.5, 23.0, 23.5, 24.0, 24.5,$  and  $25.0$ ),<sup>18</sup> the distributions of our stellar masses and the Ilbert et al. (2010) stellar masses are generally similar, with comparable median stellar masses and Kolmogorov-Smirnov test probabilities ranging from 8.0% to 49.4% that indicate similar stellar-mass distributions. Third, we compared our color-mass distribution with that in Peng et al. (2010). Figure 4 is our color-mass diagram, which is in parallel with the two bottom panels in Fig. 4 of Peng et al. (2010). The color-mass bimodality feature and the distribution of the sources in the color-mass plane in our Fig. 4 are very similar to those in Fig. 4 of Peng et al. (2010). Finally, we also estimated stellar masses utilizing the Fitting and Assessment of Synthetic Templates (FAST; Kriek et al. 2009) package that is based on galaxy SED fitting. We adopted the same stellar population synthesis model, IMF, dust-extinction law, star-formation history, and metallicity ranges as those described in § 2.1 to ensure consistency between estimates of  $z_{\text{phot}}$ , rest-frame absolute magnitudes, and stellar masses. We found that stellar masses calculated by FAST are consistent with those based on Zibetti et al. (2009) after taking into account different choices of IMFs, with an RMS of  $\lesssim 0.4$  dex, which is the typical precision of such methods. Throughout this paper, we have chosen to adopt stellar masses based on Zibetti et al. (2009) that are more directly related to source colors and rest-frame absolute magnitudes and

<sup>18</sup> For each Sample A source, we utilized a  $K$ -correction package (kcorrect.v4.1.4; Blanton & Roweis 2007) to convert the  $z_{850}$  magnitude into the  $i^+$  magnitude by convolving the best-fit SED template of the source with the  $z_{850}$  and  $i^+$  filter curves and computing the differences between the derived  $z_{850}$  and  $i^+$  magnitudes (typically  $|z_{850} - i^+| < 0.5$  mag).

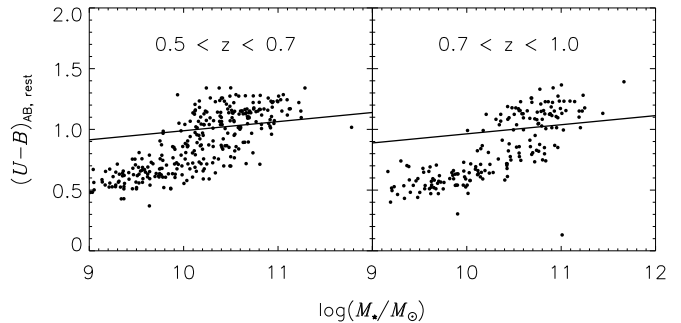


**Figure 4.** Color-mass distribution plots, for direct comparison with the two bottom panels in Fig. 4 of Peng et al. (2010) to evaluate the validity of our mass estimates. The  $y$ -axis is rest-frame  $U - B$  color (converted into the AB magnitude system), and the  $x$ -axis is the logarithm of our mass estimate reduced by 0.2 dex to adjust for the offset between our IMF (Salpeter) and the Chabrier IMF adopted in Peng et al. (2010). The solid line is the division between red and blue galaxies used by Peng et al. (2010), which is a function of  $U - B$ , mass, and redshift (see their Eq. 2). The sources used in these two panels are in the same redshift intervals as used in the two Peng et al. (2010) panels, and we also applied a magnitude cut of  $i < 22.5$  since their catalog is flux-limited at  $I < 22.5$ .

thus less dependent on model and parameter choices. We have verified that the same basic results presented below can be obtained by using stellar masses calculated with FAST.

### 3. ANALYSIS AND RESULTS

In Table 4 we present the derived source properties of the 18,035 Sample A sources. As discussed in § 1, mounting evidence has shown that luminous AGNs tend to reside in massive (i.e.,  $M_{\star} \gtrsim 10^{10} M_{\odot}$ ) and red galaxies over at least the last  $\approx 80\%$  of cosmic history, i.e.,  $z \approx 0\text{--}4$  (e.g., Barger et al. 2003; Bundy et al. 2008; Brusa et al. 2009; Silverman et al. 2009; X10; Mullaney et al. 2012). Therefore, we utilize these mass and color constraints as clues to search for the underlying population of luminous but highly obscured AGNs that are responsible for the unresolved  $\approx 20\text{--}25\%$  of the 6–8 keV XRB.

Figure 5a shows the effective color vs. mass diagram for Sample A (shown as a density map overlaid with contours), where the effective color is defined as

$$C_{\text{eff}} = (U - V)_{\text{rest}} + 0.31z + 0.08M_V + 0.51. \quad (3)$$

In Eq. 3,  $(U - V)_{\text{rest}}$  is the rest-frame  $U - V$  color (i.e.,  $M_U - M_V$ ),  $z$  is the redshift, and  $M_V$  ( $M_U$ ) is the rest-frame absolute  $V$ -band ( $U$ -band) magnitude. The definition of  $C_{\text{eff}}$  is based on the equation separating galaxies into the red sequence and the blue cloud of Bell et al. (2004), who studied the color distribution of  $\approx 25,000$   $R \lesssim 24$  galaxies with  $0.2 < z \leq 1.1$ . Taking into account a typical color scatter of  $\lesssim 0.2$  mag for the red-sequence color-magnitude relation (see § 4 of Bell et al. 2004), the Bell et al. equation separates blue and red galaxies reasonably well down to fainter magnitudes out to  $z \approx 3\text{--}4$  (e.g., X10), and thus we use  $C_{\text{eff}}$  to define whether a

**Table 4**  
Derived Properties for the Sources in Sample A

No.	RA	DEC	$z_{\text{spec}}$	$z_{\text{phot}}$	$z_{\text{ph,low}}$	$z_{\text{ph,up}}$	$M_U$	$M_B$	$M_V$	$M_{\text{reddest}}$	$F_{\text{reddest}}$	$\log(M_*/M_\odot)$
(1)	(2)	(3)	(4)	(5)	(6)	(7)	(8)	(9)	(10)	(11)	(12)	(13)
...	...	...	...	...	...	...	...	...	...	...	...	...
9000	53.11829	-27.86707	-1.000	1.620	1.548	1.707	-17.88	-17.98	-18.42	-20.15	6	8.88
9001	53.11829	-27.84127	-1.000	0.610	0.594	0.670	-15.07	-14.97	-15.59	-19.27	7	8.60
9002	53.11832	-27.81530	-1.000	0.550	0.533	0.665	-15.67	-14.98	-15.21	-17.07	7	7.26
9003	53.11834	-27.72375	-1.000	0.395	0.362	0.613	-14.85	-15.07	-15.63	-17.97	7	8.02
9004	53.11835	-27.70741	-1.000	0.750	0.605	0.863	-15.94	-15.77	-15.90	-16.42	4	7.60
...	...	...	...	...	...	...	...	...	...	...	...	...

Notes. The full table contains 18,035 entries and 20 columns for each entry. Columns: (1) Source sequence number (from 1 to 18035). (2, 3) J2000 right ascension and declination (in degrees). (4) Spectroscopic redshift ( $-1.000$  indicates no spectroscopic redshift available). (5) Photometric redshift. (6, 7)  $1-\sigma$  lower and upper limits on photometric redshift. (8, 9, 10) Rest-frame absolute  $U$ -,  $B$ -, and  $V$ -band magnitude (Vega mags). (11) Rest-frame absolute magnitude (Vega mags) that corresponds to the reddest rest-frame coverage. The conversion between Vega and AB rest-frame absolute magnitudes is:  $M_{\text{AB}} = M_{\text{Vega}} + m_{\text{conv}}$ , where  $m_{\text{conv}} = 0.628 / -0.102 / 0.029 / 0.264 / 0.501 / 0.914 / 1.381 / 1.839$  for rest-frame  $U/B/V/R/I/J/H/K$ -band, respectively; we derived these  $m_{\text{conv}}$  values using a  $K$ -correction package (kcorrect.v4.1.4; Blanton & Roweis 2007). (12) Flag of reddest rest-frame coverage. This flag shows which stellar-mass estimate is adopted as the final estimate (see § 2.3).  $F_{\text{reddest}} = (1, 2, 3, 4, 5, 6, 7)$  means that  $M_{\text{reddest}} = M_{B/V/R/I/J/H/K}$  and  $M_{B/V/R/I/J/H/K,*}$  is adopted, respectively. (13) Stellar-mass estimate adopted in this paper. (14) Stellar-mass calculated by FAST. (15, 16) CANDELS  $Y$ -band magnitude and associated  $1-\sigma$  uncertainty (AB mags;  $-99.00$  indicates no photometry available for this filter). (17, 18) CANDELS  $J$ -band magnitude and associated  $1-\sigma$  uncertainty (AB mags). (19, 20) CANDELS  $H$ -band magnitude and associated  $1-\sigma$  uncertainty (AB mags). (This table is available in its entirety in a machine-readable form in the online journal. A portion is shown here for guidance regarding its form and content.)

galaxy in Sample A is red or not<sup>19</sup> given that the sources in Sample A span a wide range in redshift and luminosity. As shown in Fig. 5a, there is a correlation between stellar mass and effective color (with large scatter) such that more massive galaxies are generally redder (i.e., having larger  $C_{\text{eff}}$  values), consistent with previous results. The normalized histograms of stellar mass and effective color are shown in Figs. 5b and 5c (black histograms), respectively. For comparison, three additional samples of highly obscured AGNs or AGN candidates are also plotted on Fig. 5a. The sample labeled with dark-green filled circles consists of 47 highly obscured AGNs at  $z \approx 0.5-3$  detected in the 6–8 keV band in the central  $6'$  area of the 4 Ms CDF-S<sup>20</sup> (their mass and color histograms are shaded in dark green in Figs. 5b and 5c; X11). The points labeled with crosses are a sample of 23 highly obscured AGN candidates at  $z \approx 0.5-1$  that were X-ray undetected and selected by their infrared star-formation rate (SFR) excess (i.e., infrared-based SFRs being a factor of  $\geq 3.2$  higher than SFRs determined from the UV after correcting for dust extinction; Luo et al. 2011). The points labeled with diamonds are a sample of 11 AGNs at  $z \approx 2$  that were  $K < 22$   $BzK$ -selected galaxies and identified as highly obscured using the 4 Ms CDF-S data (Alexan-

der et al. 2011).<sup>21</sup> As expected, the vast majority of these sources are massive and on the red sequence, the green valley, or the top of the blue cloud.

We then proceeded to stack different sub-groups of Sample A to investigate which sources produce the majority contribution to the unresolved  $\approx 20-25\%$  of the 6–8 keV XRB. We adopted the same stacking procedure as detailed in § 3.1 of Luo et al. (2011). Briefly, total counts (including background) for each individual source were extracted from an aperture  $3''$  in diameter centered on its optical position. Background counts for each source were estimated by taking the mean of the counts within 1000 apertures (also with  $3''$  diameter each), which were randomly placed within a  $1'$ -radius circle around the source avoiding any known X-ray source (i.e., outside of twice the 0.5–2 keV 90% encircled-energy aperture radius of any 4 Ms CDF-S main-catalog source). Stacked counts [total ( $S$ ) or background ( $B$ )] were the summation of counts from the stacked sample with proper aperture correction applied. The net source counts are then given by  $S - B$ , and the S/N is calculated as  $(S - B)/\sqrt{B}$  where Gaussian statistics are assumed given the large values of  $S$  and  $B$ .

Motivated by the fact that most of the obscured AGNs (and AGN candidates) appear in the massive and relatively red corner of Fig. 5a, we divided Sample A into various stellar-mass and effective-color bins and stacked the sources in each bin. Figures. 6a and 6b show the stacking results, and Table 1 gives some detailed stacking results (e.g., stacked net counts, stacked signal-to-noise ratio, effective photon index, and resolved 6–8 keV XRB fraction) for some cases of interest. It seems clear that the  $\approx 20-25\%$  unresolved 6–8 keV XRB mostly lies in galaxies with  $M_* \geq 2 \times 10^8 M_\odot$  (i.e., Sample B; see Table 1), in particular in the bin of  $2 \times 10^8 \leq M_*/M_\odot \leq 2 \times 10^9$

<sup>19</sup> Galaxies in the red sequence, the green valley, and the blue cloud have  $C_{\text{eff}} \geq 0.05$ ,  $-0.05 < C_{\text{eff}} < 0.05$ , and  $C_{\text{eff}} \leq -0.05$ , respectively, given that 0.05 is the typical “half-width” of the green valley in a color-magnitude diagram (e.g., Nandra et al. 2007; X10). By definition, we would expect the  $C_{\text{eff}}$  distribution to be double-peaked (i.e., red and blue peaks), which is, however, not clearly seen in Fig. 5c (black histogram) due to the dilution caused by color errors, uncertainties in redshift estimates, and large numbers of low-mass blue galaxies. Indeed, if we consider only, e.g., galaxies with  $0 < z < 1$  and  $M_* > 10^{9.5} M_\odot$  (as in X10), then color bimodality is clearly seen.

<sup>20</sup> These 47 AGNs are the 4 Ms CDF-S main-catalog sources that have an effective photon index of  $\Gamma_{\text{eff}} \leq 1.0$  and satisfy a binomial-probability source-selection criterion of  $P < 0.004$  in the 6–8 keV band. In X11, the  $P < 0.004$  source-detection criterion was applied only in the 0.5–8, 0.5–2, and 2–8 keV bands; here we extended the use of this criterion for 6–8 keV source detection.

<sup>21</sup> The majority of the highly obscured AGNs mentioned here have  $L_{0.5-8 \text{ keV}} < 10^{43.7} \text{ erg s}^{-1}$ , which indicates that their hosts dominate the optical-to-near infrared emission thus ensuring reliable estimates of host stellar masses and colors (see § 4.6.3 of X10 for details).



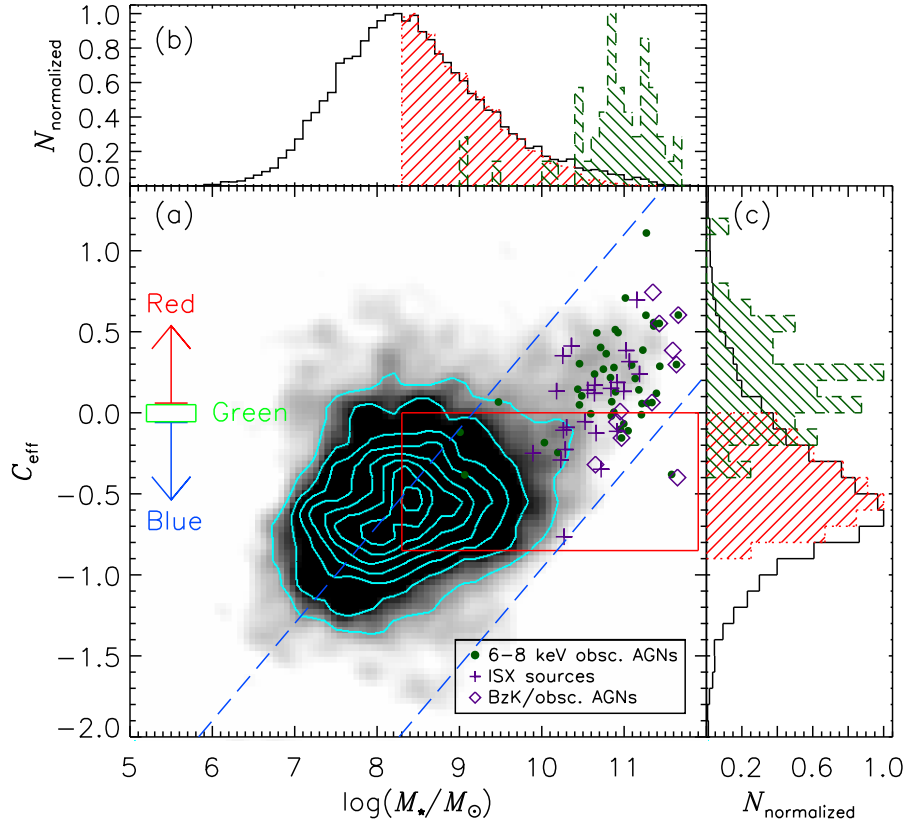


**Figure 5.** (a) Effective color-mass diagram for Sample A, which is shown as a density map overlaid with contours (the 8 contour levels are 3, 6, 9, 12, 15, 18, 21, and 24 sources per pixel). The large red rectangle highlights the region occupied by the Sample D sources. The two parallel, diagonal, long-dashed lines enclose a subsample of sources (discussed in § 4) that lie within a diagonal stripe. For comparison, a sample of 47 highly obscured AGNs detected in the 6–8 keV band in the 4 Ms CDF-S (large dark green filled circles; X11), a sample of 23 X-ray undetected and infrared-selected highly obscured AGN candidates (crosses; Luo et al. 2011), and a sample of 11 highly obscured AGNs that were  $K < 22$  BzK-selected galaxies (diamonds; Alexander et al. 2011) are also plotted (see § 3). The division scheme of the red sequence, the green valley, and the blue cloud is illustrated on the left side. (b) Normalized (peaking at unity) stellar-mass histograms for Sample A (black histogram), Sample D (red shaded histogram), and the sample of 47 highly obscured, 6–8 keV detected AGNs (dark green shaded histogram; for clarity, we do not show the histograms for the aforementioned 23 highly obscured AGN candidates and 11 highly obscured AGNs). (c) Same as Panel (b), but for normalized effective-color histograms.

where a  $2.8\sigma$  signal was obtained. Moreover, the signal also mostly arises from the Sample A sources on the top of the blue cloud, i.e., the unresolved 6–8 keV XRB has major contributions from galaxies with  $-0.85 < C_{\text{eff}} < 0$  (i.e., Sample C; see Table 1), in particular in the bin  $-0.45 < C_{\text{eff}} < 0$  where a  $2.9\sigma$  signal was obtained.

By applying both the mass and color constraints together (i.e., selecting the common sources in Sample B and Sample C), we obtained Sample D (i.e.,  $M_{\star} \geq 2 \times 10^8 M_{\odot}$  and  $-0.85 < C_{\text{eff}} < 0$ ; see Table 1). There are 6845 galaxies in Sample D that can account entirely for the unresolved  $\approx 20$ –25% of the 6–8 keV XRB (see Table 1), and the stacked 6–8 keV signal from these galaxies is significant at the  $3.9\sigma$  level (corresponding to a chance of  $p = 5.1 \times 10^{-5}$  that the signal was generated by Poisson noise). The region occupied by the Sample D sources in the effective color-mass diagram is highlighted with a large red rectangle in Fig. 5a, and their normalized stellar-mass and effective-color distributions are shown in Figs. 5b and 5c, respectively. Additional information about the stacking results for various samples can be found in Table 2 and Fig. 1.

Figure 7 shows the stacked 0.5–8 keV spectrum for the Sample D sources (open circles), with the stacked, adaptively smoothed 6–8 keV image shown as the inset. The

facts that the 6–8 keV flux is significantly elevated (compared to the fluxes in the lower-energy bands) and that there is no detection in the 4–6 keV band suggest that highly obscured AGNs dominate the stacked spectrum at high X-ray energies (see § 5.2 for more discussion). The apparent inconsistency between the hard stacked spectrum (see Fig. 7) and the relatively small band ratio (0.48, corresponding to  $\Gamma_{\text{eff}} = 1.60$ ; see Table 1) for Sample D is due to the fact that the observed 2–8 keV count rate, which dilutes the 6–8 keV contribution, is used for the calculation. We stress that this observed spectral rise at the 6–8 keV band is not caused by our sample selection, based on the following analyses: (1) The ratio between the stacked 6–8 and 4–6 keV fluxes for the parent sample, i.e., Sample A, is larger than 9, meaning that the spectral rise observed in the stacked Sample D spectrum is actually intrinsic to Sample A (see Fig. 1); (2) We stacked Sample D and non-Sample D sources in the 4–6 keV band respectively and do not find any difference between the average 4–6 keV fluxes for these two samples; (3) We examined the resolved 4–6 keV XRB fractions for Sample A sources in various stellar-mass and effective-color bins (cf. Fig. 6) and do not find any correlation or pattern between the resolved 4–6 keV XRB fractions and stellar masses/effective colors (unlike the

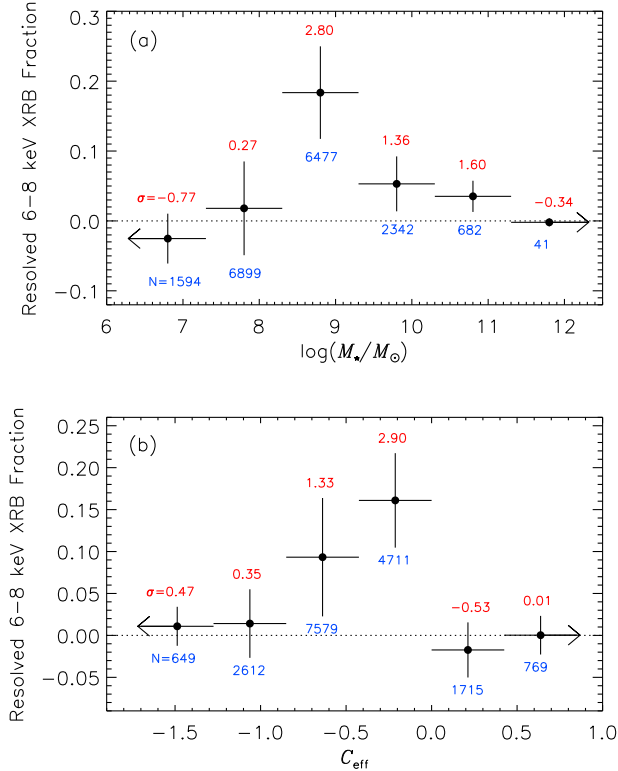


**Figure 6.** (a) Resolved 6–8 keV XRB fractions for Sample A sources in various stellar-mass bins. The number of sources ( $N$ ) and the significance (in terms of  $\sigma$ ) of the stacked signal in each stellar-mass bin are annotated accordingly. The horizontal dotted line indicates zero resolved 6–8 keV XRB fraction. (b) Same as panel (a), but for effective-color bins. Here the quoted significances are in general low due to the dilution of signal caused by sample splitting into many stacking bins (this also applies to Fig. 8).

case of Fig. 6), which suggests that, by applying our stellar-mass and effective-color cuts, we did not discard sources that have a relatively larger 4–6 keV flux.

#### 4. ROBUSTNESS OF STACKING RESULTS

It is important to assess the robustness of our stacking results and the significance of our stacked signal. Our stacking strategy, i.e., selecting sources in  $M_*$  and  $C_{\text{eff}}$  space, is strictly physically motivated, although the exact threshold values of  $M_*$  and  $C_{\text{eff}}$  were chosen for a yield of strong signal. As a result, it is possible that the significance value of  $3.9\sigma$  reported above is somewhat overestimated. Therefore, we performed 1000 10-fold cross-validation tests (Efron & Tibshirani 1993; Kohavi 1995; Davison & Hinkley 1997) to assess further the significance of our stacked signal. In each of the 10-fold cross-validation tests, we randomly split the data (i.e., Sample A) into ten subsamples of the same size. Taking one of the subsamples as the testing data, we used the rest of the subsamples as the training data upon which exploratory sample-selection criteria were utilized to find the best threshold values for  $M_*$  and  $C_{\text{eff}}$  in a similar way to the construction of Sample D.<sup>22</sup> These threshold values were then used for selecting sources from the test-

<sup>22</sup> We required that the grid in  $\log M_* - C_{\text{eff}}$  space used to find the threshold values be not finer than 0.3 dex for  $\log M_*$  or 0.05 for  $C_{\text{eff}}$ , which are the typical errors on  $M_*$  or  $C_{\text{eff}}$ .

ing subsample. The process was repeated with each of the ten subsamples being the testing data once, and in the end all the selected sources in these ten folds were combined for stacking, which provided one estimate of the significance of our stacked signal ( $\sigma_s$ ). The 10-fold cross-validation test was performed 1000 times, and a distribution for  $\sigma_s$  was obtained. The median value for  $\sigma_s$  is 3.3 (corresponding to a chance of  $p = 5.0 \times 10^{-4}$  of the signal coming from pure Poisson noise). This value is likely to be slightly pessimistically biased because the effectiveness of the search for the best threshold  $M_*$  and  $C_{\text{eff}}$  values is highly dependent on the training sample size, whereas in 10-fold cross validation tests 10% of the data were not used for training (Kohavi 1995). Therefore, the true significance of our stacked signal should be between  $3.3\sigma$  and  $3.9\sigma$ .

We also performed several other robustness and consistency tests. For example, we stacked randomly selected sets of 6845 sources from Sample A. We repeated this procedure 10,000 times and find not a single case where the stacked 6–8 keV signal resolves more XRB or has higher significance compared to Sample D. This is consistent with our reported significance of  $(3.3\text{--}3.9)\sigma$  with  $p = (5.1\text{--}50) \times 10^{-5}$ . We also stacked all the non Sample D sources (i.e.,  $18035 - 6845 = 11190$  sources) and find that the stacked 6–8 keV signal is, as expected, consistent with background (a  $0.1\sigma$  signal). We furthermore investigated the effects of changes in the sample-selection criteria on our stacking results. We considered various combinations of stellar-mass and effective-color threshold values [e.g.,  $M_{*,\text{threshold}}$  varying between  $(1\text{--}5) \times 10^8 M_\odot$  and the lower and upper  $C_{\text{eff}}$  threshold values varying by  $\pm 0.2$ , respectively] and obtained similar stacking results to that of Sample D in all cases.

Finally, we have explored another purely physically motivated stacking strategy, which is formulated upon observation of the distribution of the three groups of obscured AGNs or AGN candidates in Fig. 5a. Given the locations of these obscured AGNs or AGN candidates in the figure, we selected sources lying within a diagonal stripe,  $5.5 < 0.6 \log M_* - C_{\text{eff}} < 7.0$  (i.e., the region enclosed by the two parallel, diagonal, long-dashed lines in Fig. 5a). This stripe, running from the upper right corner to the lower left in Fig. 5a, is essentially the narrowest stripe containing all the obscured AGNs or AGN candidates except two “outliers” that are located around the  $C_{\text{eff}} \approx -0.4$  and  $\log M_* > 11$  area. There are 8415 sources within this stripe, and they contribute  $25.9 \pm 7.6\%$  to the unresolved 6–8 keV XRB (a  $3.5\sigma$  stacked signal).

## 5. DISCUSSION

### 5.1. General Properties of the Galaxies Hosting the Underlying Highly Obscured AGNs

Given that the Sample D sources can account for the unresolved  $\approx 20\text{--}25\%$  of the 6–8 keV XRB, it is of interest to determine what sources provide the majority contributions, i.e., what sources in Sample D are most likely to host “hidden” highly obscured AGNs. We therefore examined the resolved 6–8 keV XRB fractions for the Sample D sources in various redshift and  $z$ -band magnitude bins, as shown in Figs. 8a and 8b, respectively. It appears that the galaxies with redshifts  $1 \lesssim z \lesssim 3$  (see Fig. 8a) and magnitudes  $z_{850} \approx 25\text{--}28$  (see Fig. 8b)

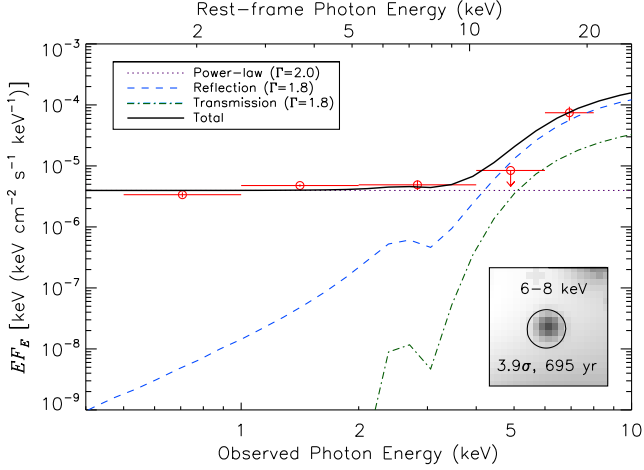


**Figure 7.** Stacked X-ray spectrum (open circles) for the 6845 sources in Sample D (the top  $x$ -axis shows the rest-frame photon energy at  $z = 1.6$ , which is the median redshift of the Sample D sources; see Table 1). The downward arrow in the 4–6 keV band indicates a  $3\sigma$  upper limit. The solid curve is a schematic fit to the stacked X-ray spectrum, which is the sum of three components (each evaluated at  $z = 1.6$ ): an unabsorbed power-law component accounting for star formation (dotted line;  $\Gamma = 2.0$ ), a pure reflection component from the AGN (dashed curve), and a pure transmission component from the AGN (dashed-dot curve). *Inset:* Stacked, adaptively smoothed, 6–8 keV image, with the  $3''$  diameter photometric aperture, the significance of the stacked signal, and the total stacked exposure shown.

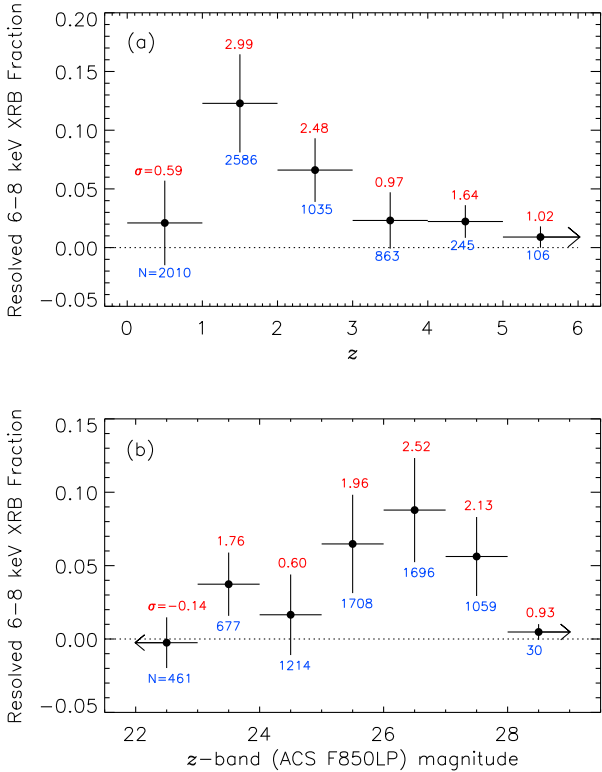


**Figure 8.** (a) Resolved 6–8 keV XRB fractions for Sample D sources in various redshift bins (cf. Fig. 6). (b) Same as Panel (a), but for  $z$ -band magnitude bins.

make the major contributions to the unresolved 6–8 keV XRB, thus being more likely to host the highly obscured AGNs that escape from even the deepest *Chandra* obser-

vations. Marchesini et al. (2012) studied the rest-frame  $V$ -band luminosity function of galaxies at  $0.4 \leq z < 4.0$ . Based on best-fit  $M_V^*$  values (for a Schechter luminosity function) in the different redshift ranges presented in their Table 2, we estimate that the above Sample D sources with  $z_{850} \approx 25$ –28 at  $1 \lesssim z \lesssim 3$  typically have  $(0.05$ – $0.10) L_V^*$ . Here we do not expect cosmic variance induced by large-scale structures (LSS) to affect the basic redshift distribution observed in Fig. 8a (thus affecting our basic results) in a significant way because of the following (also see § 1 for a brief discussion of cosmic variance): (1) All known prominent LSS in the CDF-S has  $z < 1$  (i.e.,  $z_{\text{LSS}} = 0.67$  and  $0.73$ ; see, e.g., Silverman et al. 2010, and their Fig. 11 where small enhancements at other redshifts can also be seen); and (2) The broad redshift bins ( $\Delta z = 1$ ) that we considered in Fig. 8a and the broad redshift range ( $1 \lesssim z \lesssim 3$ ) where we find most of the signal should be, by design, relatively insensitive to the effects of cosmic variance induced by LSS.

As described in § 3, three additional samples of highly obscured AGNs or AGN candidates are also shown in the effective color-mass diagram (Fig. 5a), which are seen to be massive and relatively red. This motivates and supports our utilization of the mass and color constraints as clues in identifying a source population (i.e., Sample D) responsible for the unresolved 6–8 keV XRB.<sup>23</sup> Nevertheless, the hosts of these highly obscured AGNs or AGN candidates are much more massive and redder than the Sample D sources (see Figs. 5a–5c). In particular, the stellar masses of the Sample D sources appear notably low (most having  $2 \times 10^8 \lesssim M_*/M_\odot \lesssim 2 \times 10^9$ ) with a median stellar mass of  $\approx 8 \times 10^8 M_\odot$ . However, for a typical star-forming galaxy with  $M_* = 8 \times 10^8 M_\odot$  at  $z = 1.6$  (the median redshift of the Sample D sources), its stellar mass will grow by a factor of  $\approx 4$ – $50$  by the present day, which places its  $z = 0$  stellar mass at  $\approx 0.1$ – $1$  times the stellar mass of the Milky Way ( $\approx 5 \times 10^{10} M_\odot$ ; e.g., Hammer et al. 2007). The above estimate of mass-growth factor was made based on the calculations done by Leitner (2012) and equations 1 and 21 in Peng et al. (2010) taking into account the effects of mergers and merger-induced quenching. This predicted stellar-mass growth appears consistent with the fact that Lyman-alpha emitters with a typical stellar mass of  $\sim 10^8$ – $10^9 M_\odot$  at  $z \sim 2$ – $3$  are thought to grow into galaxies about as massive as the Milky Way by the present day (Gawiser et al. 2007; Guaita et al. 2010). Such a significant stellar-mass growth would imply a very large reservoir of gas present to sustain a large amount of star formation since  $z = 1.6$ . In addition to supporting star formation, this gas at  $z = 1.6$  may also feed the supermassive black hole (SMBH; explaining the common accretion likely present in Sample D) and obscure the SMBH (explaining the high obscured AGN fraction apparently seen in Sample D; see § 5.2.2 for details). Most of the Sample D sources are brighter than  $z_{850} \approx 27$ ,

<sup>23</sup> We note that the 6–8 keV signal is weak for the X-ray undetected sources with  $M_* > 10^{10} M_\odot$  (the resolved fraction is  $3.0\% \pm 2.8\%$  with  $\sigma = 1.1$ ), which could potentially be the more heavily obscured counterparts of the X-ray detected highly obscured AGNs (see Fig. 5a). We speculate that there are simply not enough objects to produce a significant signal for such massive galaxies.

thus having reasonably good photometric coverage (over 99% of the sources in Sample D have detections in at least 9 bands), so their photometric-redshift and stellar-mass estimates are of sufficient quality for our study (see § 2.1 and § 2.3). The above results therefore imply that there are a significant number of highly obscured AGNs that are hosted by relatively low-mass galaxies ( $2 \times 10^8 \lesssim M_*/M_\odot \lesssim 2 \times 10^9$ ) at  $1 \lesssim z \lesssim 3$ .<sup>24</sup>

Such an AGN population might seem surprising given that the majority of the X-ray detected AGNs reside in massive galaxies. We thus discuss in § 5.2 constraints upon these underlying highly obscured AGNs and their parent population.

## 5.2. Constraints upon Underlying Highly Obscured AGNs and Their Parent Population

### 5.2.1. Spectral constraints

At  $z = 1.6$ , which is the median redshift of the Sample D sources, moderately Compton-thick obscuring material ( $N_{\text{H}} > 1.5 \times 10^{24} \text{ cm}^{-2}$ ) would be required to absorb X-rays strongly up to rest-frame  $\approx 16 \text{ keV}$ , but then permit higher energy emission to penetrate through the material. In this regime, performing an absorption correction to derive a typical luminosity is difficult and geometry dependent (and thus subject to large uncertainties). However, based on results for local Seyfert galaxies (e.g., Guainazzi et al. 2000) and utilizing the MYTORUS model (Murphy & Yaqoob 2009),<sup>25</sup> we would expect typical column densities of  $N_{\text{H}} \approx 4 \times 10^{24} \text{ cm}^{-2}$ . Due to the Compton-thick nature of the sources on average, and the fact that there are surely many star-forming galaxies in Sample D, the stacked X-ray spectrum (with a measured  $\Gamma_{\text{eff}} = 1.60 \pm 0.16$  that is derived from the stacked band ratio,  $0.48 \pm 0.08$ ; see Table 1) will be affected by both Compton-thick AGN emission and star-formation emission. The quality of the stacked X-ray spectrum does not allow for a proper fit, but an illustrative fit is sufficiently useful for our purposes here, which is shown as the solid curve in Fig. 7. This is the sum of three components (each evaluated at  $z = 1.6$ ): an unabsorbed power-law representing the star-formation component (dotted line; the POWERLAW model in XSPEC<sup>26</sup> with  $\Gamma = 2.0$ ), a Compton-reflection component from the AGN (dashed curve), and a transmission component from the AGN (dashed-dot curve). The latter two AGN components (reflection and transmission) were obtained with a MYTORUS model with  $N_{\text{H}} = 4 \times 10^{24} \text{ cm}^{-2}$  (see Footnote 25 for the values of other parameters). It is clear that (1) the reflection component dominates the 6–8 keV emission (cf. a composite, reflection-dominated

spectrum for a sample of highly obscured AGNs at  $z \approx 2$  obtained by Alexander et al. 2011; see their Fig. 5), being a factor of  $\approx 4$  larger than the transmission component; and (2) the unabsorbed power-law component dominates the 0.5–4 keV emission.

### 5.2.2. Constraints upon AGN fraction

A quantity of interest is the AGN fraction ( $f_{\text{AGN}}$ ) in a parent sample of galaxies. While the determination of  $f_{\text{AGN}}$  is challenging, there have been some previous attempts for, e.g., samples of galaxies that include X-ray-detected AGNs. For example, X10 estimated  $f_{\text{AGN}} \approx 10\%$  for moderate-luminosity ( $L_{0.5-8 \text{ keV}} \approx 10^{41.9-43.7} \text{ erg s}^{-1}$ ) AGNs at  $z \approx 0-3$  in a parent sample of galaxies with  $M_* \geq 10^{10.3} M_\odot$ . Recently Aird et al. (2012) studied a sample of 2–10 keV selected AGNs and their parent sample of galaxies that have  $0.2 < z < 1.0$  and  $3 \times 10^9 < M_*/M_\odot < 10^{12}$ . They found that the incidence of AGN can be defined by a universal Eddington-ratio distribution that is independent of the host-galaxy stellar mass and has a power-law form with the slope being  $-0.65$  and the normalization evolving strongly with redshift [ $\propto (1+z)^{3.8}$ ]. Their results, if applicable down to lower mass galaxies and for AGNs up to higher redshifts, would yield an estimate of  $f_{\text{AGN}} \approx 10\%$  for AGNs of  $L_{2-10 \text{ keV}} \approx 10^{41-44} \text{ erg s}^{-1}$  in galaxies with  $M_* \approx 10^9 M_\odot$  at  $z \approx 1-3$ .

The above estimates of  $f_{\text{AGN}} \approx 10\%$  appear to satisfy the 6–8 keV non-detection requirement of individual hidden AGNs in Sample D. The 6845 Sample D sources have a total stacked 6–8 keV flux of  $3.5 \times 10^{-14} \text{ erg cm}^{-2} \text{ s}^{-1}$ . Assuming this total flux is produced uniformly from a fraction  $f_{\text{AGN}}$  of the Sample D sources (corresponding to an observed sky density of  $\approx 2.5 \times 10^5 f_{\text{AGN}} \text{ deg}^{-2}$  given a stacking area of  $0.027 \text{ deg}^2$ ; see § 2), we obtain an average 6–8 keV flux,  $5.1 \times 10^{-18} f_{\text{AGN}}^{-1} \text{ erg cm}^{-2} \text{ s}^{-1}$ , for the hidden AGNs in Sample D. The on-axis 6–8 keV sensitivity limit in the 4 Ms CDF-S is  $\approx 2 \times 10^{-16} \text{ erg cm}^{-2} \text{ s}^{-1}$ . If it is assumed that these hidden sources are just below the 6–8 keV detection threshold, then the non-detection in this band requires  $5.1 \times 10^{-18} f_{\text{AGN}}^{-1} < 2 \times 10^{-16}$ , i.e.,  $f_{\text{AGN}} > 2.6\%$ , indicating  $> 170$  AGNs in Sample D. Another estimate of a lower limit on  $f_{\text{AGN}}$  can be obtained through population-synthesis models. For instance, the Gilli et al. (2007) model predicts that there are  $\approx 150$  obscured (i.e.,  $N_{\text{H}} \gtrsim 10^{22} \text{ cm}^{-2}$ ) AGNs with 0.5–2 keV rest-frame intrinsic luminosities greater than  $10^{42} \text{ erg s}^{-1}$  not detected in the central  $6'$ -radius area of the 4 Ms CDF-S, and that  $\approx 30-50\%$  of these missing AGNs are highly obscured (i.e.,  $N_{\text{H}} \gtrsim 3 \times 10^{23} \text{ cm}^{-2}$ ). This predicted fraction of obscured AGNs,  $\approx 150/6845 \approx 2.2\%$  for Sample D, is likely a lower limit since the population-synthesis model of Gilli et al. (2007) does not take into account low-luminosity AGNs (i.e.,  $L_{0.5-2 \text{ keV}} < 10^{42} \text{ erg s}^{-1}$ ) that tend to be hosted by low-mass galaxies. Therefore, the number of missing AGNs in Sample D could potentially be up to several hundred.

In addition to  $f_{\text{AGN}}$ , another quantity of interest is the obscured AGN fraction. As discussed in § 5.2.1, the majority of the underlying AGNs in Sample D need to be highly obscured in order to produce the steep 6–8 keV rise in the stacked Sample D spectrum; this result sug-

<sup>24</sup> The wording of “relatively low-mass” here means that the Sample D sources have low masses when compared to the aforementioned highly obscured AGNs or AGN candidates. They do, of course, still have high masses when compared to the large number of non-Sample D sources (see Figs. 5a and 5b).

<sup>25</sup> We used a model that consists of the transmitted continuum, the scattered (i.e., reflection) continuum, and no emission lines. In the model we adopted  $\Gamma = 1.8$ ,  $z = 1.6$ , an inclination angle of  $90^\circ$ , and a varying  $N_{\text{H}}$  (other parameters were fixed to their default values). We found that a column density of  $N_{\text{H}} \approx 4 \times 10^{24} \text{ cm}^{-2}$  leads to a ratio of  $\approx 5$  between the observed 6–8 and 4–6 keV energy output (represented by the  $EF_E$  values).

<sup>26</sup> XSPEC is an X-ray spectral fitting package (Arnaud 1996) that is available at <http://heasarc.nasa.gov/xanadu/xspec/>.



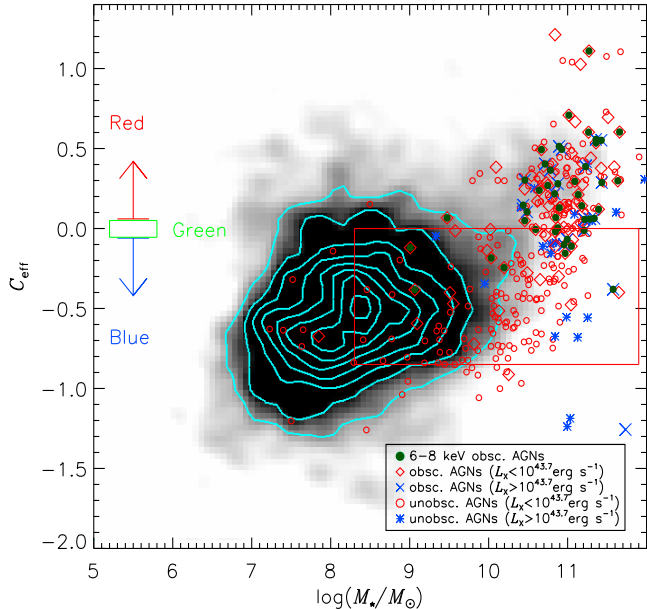


**Figure 9.** Same as Fig. 5a, but including the unobscured (i.e., having  $\Gamma_{\text{eff}} > 1$ ) and obscured (i.e., having  $\Gamma_{\text{eff}} < 1$ ) AGNs in the central  $6'$  area of the 4 Ms CDF-S. A small fraction of the AGNs are luminous (i.e.,  $L_{0.5-8\text{keV}} > 10^{43.7} \text{ erg s}^{-1}$ ), so the color and stellar-mass estimates of their hosts are subject to AGN contamination; however, this does not affect our discussion here (see text).

gests that the obscured AGN fraction should be close to  $f_{\text{AGN}}$  for Sample D. We show in Fig. 9 the effective color-mass diagram for the unobscured (i.e., having  $\Gamma_{\text{eff}} > 1$ ) and obscured (i.e., having  $\Gamma_{\text{eff}} < 1$ ) AGNs detected in the central  $6'$  area of the 4 Ms CDF-S. It seems clear from the figure that the fraction of X-ray detected sources decreases toward lower masses regardless of whether the X-ray sources are obscured or unobscured. In the stellar-mass range ( $2 \times 10^8 \lesssim M_*/M_\odot \lesssim 2 \times 10^9$ ) where most of the stacked 6–8 keV signal lies, there are only about 10 X-ray detected unobscured AGNs (and only 3 of them have  $1 \lesssim z \lesssim 3$ ). An order-of-magnitude estimate of the percentage of highly obscured AGNs among the underlying AGN population in Sample D would then be  $1 - [3/(6845 \times f_{\text{AGN}})] > 90\%$ . This percentage of highly obscured AGNs appears high when compared to available attempts at measurement of this quantity as a function of X-ray luminosity and redshift (e.g., Treister & Urry 2006; Hasinger et al. 2008; Gilli et al. 2010); see § 5.2.3 for estimation of the typical X-ray luminosities of our sources. However, the available attempted measurements have significant systematic uncertainties owing to selection incompleteness, limited source spectral characterization, and other issues. Furthermore, as is clear from Fig. 5, we are investigating distant AGN activity in a quite different regime from that where the luminosity and redshift dependences of the obscured percentage have been studied, so past results may not be applicable.

### 5.2.3. Constraints upon X-ray luminosity, black-hole mass, and host stellar mass

As estimated earlier, we obtain an average 6–8 keV flux of  $5.1 \times 10^{-18} f_{\text{AGN}}^{-1} \text{ erg cm}^{-2} \text{ s}^{-1}$  for the hidden AGNs in Sample D. Adopting a reasonable absorption correction for a column density of  $N_{\text{H}} = 4 \times 10^{24} \text{ cm}^{-2}$

within the MYTORUS model (see Footnote 25 for the adopted model parameters), we estimate the average 2–10 keV rest-frame intrinsic luminosity to be  $4.0 \times 10^{42} f_{\text{AGN}}^{-1} \text{ erg s}^{-1}$  (assuming  $z = 1.6$ ). Given the corresponding average 2–10 keV rest-frame absorbed luminosity  $2.0 \times 10^{41} f_{\text{AGN}}^{-1} \text{ erg s}^{-1}$ , the ratio between the absorbed and intrinsic 2–10 keV luminosities is therefore  $(2.0 \times 10^{41}) / (4.0 \times 10^{42}) \approx 5.0\%$ . This ratio for Compton-thick AGNs is strongly dependent upon the precise measurement of absorption, which is difficult and thus renders this ratio uncertain (see, e.g., Comastri 2004 for a review).

Taking  $f_{\text{AGN}} = 10\%$  and assuming a 2–10 keV bolometric correction of 10 (e.g., Vasudevan et al. 2009, 2010; Lusso et al. 2011), we estimate the average bolometric luminosity of the highly obscured AGNs hidden in Sample D to be  $4.0 \times 10^{44} \text{ erg s}^{-1}$ , which implies that the masses of the relevant SMBH are  $> 3.1 \times 10^6 M_\odot$  if they accrete at a sub-Eddington level. We assume  $M_* \sim M_{\text{bulge}}$  for simplicity and obtain a correlation of  $M_{\text{BH}}/M_* \approx 1/500$  in the local universe based on the results of Marconi & Hunt (2003). There are studies indicating that the average SMBH to host-galaxy mass ratio evolves positively with redshift (e.g., Woo et al. 2008; Merloni et al. 2010); however, such studies are subject to large uncertainties (e.g., Jahnke et al. 2009; Shen & Kelly 2010). Here we take an evolution form of  $M_{\text{BH}}/M_* \propto (1+z)^{0.68}$  (Merloni et al. 2010) and obtain a correlation of  $M_{\text{BH}}/M_* \approx (1/500) \times (1+1.6)^{0.68} \approx 1/250$  at  $z = 1.6$ , which then implies a typical stellar mass of  $M_* > 7.8 \times 10^8 M_\odot$  for the hosts of the highly obscured AGNs hidden in Sample D. This  $M_* > 7.8 \times 10^8 M_\odot$  constraint is just consistent with the median stellar mass of Sample D ( $8.1 \times 10^8 M_\odot$ ; see Table 1). However, there will be a mis-match between the estimated SMBH mass and the typical host stellar mass, if a lower  $f_{\text{AGN}}$  value or a lower ratio between the absorbed and intrinsic 2–10 keV luminosities is assumed.

### 5.2.4. Constraints upon star-forming galaxies

As shown in Fig. 7, the 0.5–2 keV stacked X-ray emission of Sample D appears to be dominated by an unabsorbed power-law component that is likely associated with star-formation related processes. The Sample D sources have a total 0.5–2 keV flux of  $9.8 \times 10^{-15} \text{ erg cm}^{-2} \text{ s}^{-1}$ ; the corresponding average 0.5–2 keV flux,  $1.43 \times 10^{-18} \text{ erg cm}^{-2} \text{ s}^{-1}$ , is a factor of  $\approx 6$  below the on-axis 0.5–2 keV sensitivity limit in the 4 Ms CDF-S (X11). We estimated absorption-corrected factors in the 0.5–2, 0.5–8, and 2–10 keV bands using a ZPOWERLW×ZWABS×WABS model in XSPEC, where  $z = 1.6$ ,  $\Gamma = 2.0$ , and intrinsic  $N_{\text{H}} = 10^{20} \text{ cm}^{-2}$ . We then estimated the average 0.5–2, 0.5–8, and 2–10 keV rest-frame intrinsic luminosities to be  $2.6 \times 10^{40}$ ,  $5.2 \times 10^{40}$ , and  $3.0 \times 10^{40} \text{ erg s}^{-1}$ , respectively. Using these luminosities, we obtained SFR estimates of  $5.7 M_\odot \text{ yr}^{-1}$  based on the Ranalli et al. (2003) relation between SFR and  $L_{0.5-2 \text{ keV}}$  (see their Eq. 14),  $21.8 M_\odot \text{ yr}^{-1}$  based on the Lehmer et al. (2010) relation between SFR and  $L_{2-10 \text{ keV}}$  (see the fourth line in their Table 4),  $19.9 M_\odot \text{ yr}^{-1}$  based on the Mineo et al. (2012) relation between SFR and  $L_{0.5-8 \text{ keV}}$  (see their Eq. 22), and  $4.2 M_\odot \text{ yr}^{-1}$  based on the Vattakunnel et al. (2012) relation between SFR

and  $L_{2-10\text{ keV}}$  (see their Eq. 6), respectively, assuming that the mentioned relations also apply at lower stellar masses and higher redshifts. Based on the SFRs derived above and the mean stellar mass of the Sample D sources ( $3.2 \times 10^9 M_\odot$ ), we estimate specific SFRs (sSFR, i.e., SFR per stellar mass) ranging from  $1.3 \text{ Gyr}^{-1}$  to  $6.8 \text{ Gyr}^{-1}$ . These estimated sSFRs are on the same order of magnitude as an estimate of  $2.0 \text{ Gyr}^{-1}$  made using Eq. 1 of Peng et al. (2010) that was obtained based on observations of typical star-forming galaxies at  $z \approx 0-2$ , with the input values of  $3.2 \times 10^9 M_\odot$  and  $z = 1.6$ . We note that the above relations between SFR and X-ray luminosities are subject to large uncertainties, with typical scatters of 0.4–0.5 dex.

### 5.3. Supporting Evidence for Relatively Low-Mass Galaxies Hosting Highly Obscured AGNs

Our finding, that there is an appreciable fraction of relatively low-mass galaxies that host highly obscured AGNs at  $z \approx 1-3$ , is somewhat unexpected. Nevertheless, there is already some supporting evidence, i.e., there are potential analogs both in the distant and nearby universe. For example, Trump et al. (2011) identified apparent weak and/or obscured AGN activity in a sample of 28 X-ray undetected, low-mass ( $M_{\star, \text{median}} \approx 3 \times 10^9 M_\odot$ ),  $z \approx 2$  emission-line galaxies in the GOODS-S region,<sup>27</sup> suggesting that AGNs may be common in relatively low-mass star-forming galaxies at  $z \approx 2$ . Further near-infrared spectroscopic observations are needed to identify larger samples of highly obscured AGNs in relatively low-mass galaxies at high redshifts. However, as demonstrated by Goulding & Alexander (2009) and Goulding et al. (2010), even in the nearby universe significant mass accretion onto SMBHs could be missed in the most sensitive optical surveys due to absent or weak optical AGN signatures caused by extinction. Locally, a recent study revealed a *Chandra*-detected, moderately obscured ( $N_{\text{H}} \approx 6 \times 10^{22} \text{ cm}^{-2}$ ) AGN that may have  $M_{\text{BH}} \sim 2 \times 10^6 M_\odot$  residing in a dwarf galaxy (Henize 2-10) with  $M_\star \approx 3.7 \times 10^9 M_\odot$  (Reines et al. 2011).

### 5.4. Future Prospects

As discussed earlier, there are likely at least several hundred highly obscured AGNs hidden in Sample D. If we could better isolate this population of missing AGNs, we would be able to boost significantly the 6–8 keV stacked signal. One possibility for achieving a better stacked signal would be to obtain improved photometry that extends to the key rest-frame *K*-band or beyond. Such improved photometry will lead to more reliable stellar-mass estimates, which will consequently result in a more efficient sample selection and a likely boost in the stacked signal. The Mid-InfraRed Instrument (MIRI;

Swinyard et al. 2004; Wright et al. 2004) onboard the James Webb Space Telescope (*JWST*; Gardner et al. 2006) will be able to provide near- and mid-IR data that are greatly superior to the *Spitzer* IRAC data currently in use. The limiting magnitudes of MIRI (for the same length of exposure and the same signal-to-noise ratio) go deeper by over 2 magnitudes than those of IRAC. This means that all of our Sample A sources (compared to  $\approx 60\%$  currently) will have rest-frame *K*-band coverage or beyond with photometric quality significantly better than that at present. Other possibilities for increasing the stacked signal by, for instance, identifying AGN candidates through morphologies or through deep optical and near-infrared spectroscopic observations (where the CANDELS imaging and *JWST* spectroscopic data would be most critical), remain of interest, but are beyond the scope of this work.

One might think that future hard X-ray missions such as *NuSTAR* and *ASTRO-H* would be able to detect such highly obscured AGNs hidden in relatively low-mass galaxies. In the distant universe ( $z \gtrsim 0.5$ ), however, *NuSTAR* and *ASTRO-H* simply do not have sufficient sensitivity to make such direct detections (e.g., Luo et al. 2011). In contrast, a 10 Ms CDF-S has the potential of detecting a fraction of such highly obscured AGNs if at least some of these hidden sources are not too far below the 6–8 keV detection threshold of the 4 Ms CDF-S. Furthermore, a 10 Ms CDF-S would also increase the signal-to-noise ratios of the stacking results and thus complement the aforementioned approaches of improved sample selection.

We thank the referee for helpful feedback that improved this work. We thank T. Dahlen for providing the GOODS-S *HST* *z*-band selected photometric catalog, J. R. Mullaney and M. Pannella for making comparisons between stellar-mass estimates, and R. Ciardullo and C. Gronwall for helpful discussions. Support for this work was provided by NASA through *Chandra* Award SP1-12007A (YQX, SXW, WNB) issued by the *Chandra* X-ray Observatory Center, which is operated by the Smithsonian Astrophysical Observatory, and by NASA ADP grant NNX10AC99G (YQX, SXW, WNB). We also acknowledge the financial support of the Youth 1000 Plan (QingNianQianRen) program and the USTC startup funding (YQX), the Science and Technology Facilities Council (DMA), *Chandra* Award SP1-12007B (FEB), the Programa de Financiamiento Basal (FEB), the CONICYT-Chile grants FONDECYT 1101024 and fondap-cata 15010003 (FEB), the Italian Space Agency (ASI) under the ASI-INAF contract I/009/10/0 (AC, RG, CV), and the Einstein Fellowship Program (BDL).

## REFERENCES

Aird, J. et al. 2012, *ApJ*, 746, 90

<sup>27</sup> Of the Trump et al. (2011) sample of 28 galaxies, 26 (14) are included in our Sample A (Sample D) and the other 2 are not included due to their vicinity to the 4 Ms CDF-S sources. Of these 26 (14) common Sample A (Sample D) sources, our estimates of  $z_{\text{phot}}$  and stellar mass for 18 (11) sources are in reasonable agreement with the Trump et al. (2011) estimates.

Alexander, D. M. et al. 2003, *AJ*, 126, 539  
 Alexander, D. M. et al. 2011, *ApJ*, 738, 44  
 Arnaud, K. A. 1996, *ASPC*, 101, 17  
 Barger, A. J., Cowie, L. L., Brandt, W. N., Capak, P., Garmire, G. P., Hornschemeier, A. E., Steffen, A. T., & Wehner, E. H. 2002, *AJ*, 124, 1839  
 Barger, A. J., et al. 2003, *AJ*, 126, 632  
 Barger, A. J., Cowie, L. L., Mushotzky, R. F., Yang, Y., Wang, W.-H., Steffen, A. T., & Capak, P. 2005, *AJ*, 129, 578



- Bauer, F. E., Alexander, D. M., Brandt, W. N., Schneider, D. P., Treister, E., Hornschemeier, A. E., & Garmire, G. P. 2004, *AJ*, 128, 2048
- Bell, E. F., & de Jong, R. S. 2000, *MNRAS*, 312, 497
- Bell, E. F. et al. 2004, *ApJ*, 608, 752
- Bertin, E., & Arnouts, S. 1996, *A&AS*, 117, 393
- Blanton, M. R., & Roweis, S. 2007, *AJ*, 133, 734
- Brandt, W. N. et al. 2000, *AJ*, 119, 2349
- Brandt, W. N. et al. 2001, *AJ*, 122, 2810
- Brandt, W. N., & Alexander, D. M. 2010, *PNAS*, 107, 7184
- Brandt, W. N., & Hasinger, G. 2005, *ARA&A*, 43, 827
- Brusa, M. et al. 2009, *A&A*, 507, 1277
- Bruzual, G., & Charlot, S. 2003, *MNRAS*, 344, 1000
- Bundy, K. et al. 2008, *ApJ*, 681, 931
- Calzetti, D., Armus, L., Bohlin, R. C., Kinney, A. L., Koornneef, J., & Storchi-Bergmann, T. 2000, *ApJ*, 533, 682
- Cappelluti, N. et al. 2012, *MNRAS*, accepted (arXiv:1208.4105)
- Cardamone, C. N. et al. 2010, *ApJS*, 189, 270
- Chabrier, G. 2003, *PASP*, 115, 763
- Comastri, A. 2004, in *Supermassive Black Holes in the Distant Universe*, ed. A. J. Barger (Astrophysics and Space Science Library, Vol. 308; Dordrecht: Kluwer), 245
- Comastri, A. et al. 2011, *A&A*, 526, L9
- Cowie, L. L., Garmire, G. P., Bautz, M. W., Barger, A. J., Brandt, W. N., & Hornschemeier, A. E. 2002, *ApJ*, 566, L5
- Dahlen, T. et al. 2010, *ApJ*, 724, 425
- Davison, A. C., & Hinkley, D. V. 1997, *Bootstrap Methods and Their Application*, Cambridge Series in Statistical and Probabilistic Mathematics (Cambridge University Press)
- Efron, B., & Tibshirani, R. 1993, *An Introduction to the Bootstrap*, Monographs on Statistics and Applied Probability (Chapman & Hall)
- Feldmann, R. et al. 2006, *MNRAS*, 372, 565
- Feruglio, C., Daddi, E., Fiore, F., Alexander, D. M., Piconcelli, E., & Malacaria, C. 2011, *ApJ*, 729, L4
- Gardner, J. P. et al. 2006, *SSRv*, 123, 485
- Gawiser, E. et al. 2007, *ApJ*, 671, 278
- Giacconi, R. et al. 2002, *ApJS*, 139, 369
- Gilli, R. et al. 2003, *ApJ*, 592, 721
- Gilli, R. et al. 2005, *A&A*, 430, 811
- Gilli, R., Comastri, A., & Hasinger, G. 2007, *A&A*, 463, 79
- Gilli, R., Comastri, A., Vignali, C., Ranalli, P., & Iwasawa, K. 2010, *AIPC*, 1248, 359
- Gilli, R. et al. 2011, *ApJ*, 730, L28
- Goulding, A. D., & Alexander, D. M. 2009, *MNRAS*, 398, 1165
- Goulding, A. D., Alexander, D. M., Lehmer, B. D., & Mullaney, J. R. 2010, *MNRAS*, 406, 597
- Grogin, N. A. et al. 2011, *ApJS*, 197, 35
- Guainazzi, M., Matt, G., Brandt, W. N., Antonelli, L. A., Barr, P., & Bassani, L. 2000, *A&A*, 356, 463
- Guaita, L. et al. 2010, *ApJ*, 714, 255
- Hammer, F., Puech, M., Chemin, L., Flores, H., & Lehnert, M. D. 2007, *ApJ*, 662, 322
- Hasinger, G. 2008, *A&A*, 490, 905
- Hickox, R. C., & Markevitch, M. 2006, *ApJ*, 645, 95
- Ilbert, O. et al. 2010, *ApJ*, 709, 644
- Jahnke, K. et al. 2009, *ApJ*, 706, L215
- Johnson, H. L., & Morgan, W. W. 1953, *ApJ*, 117, 313
- Koekemoer, A. M. et al. 2011, *ApJS*, 197, 36
- Kohavi, R. 1995, in *Proceedings IJCAI-95*, ed. C.S. Mellish (Los Altos, CA: Morgan Kaufmann), 1137
- Komatsu, E. et al. 2011, *ApJS*, 192, 18
- Kriek, M., van Dokkum, P. G., Labbé, I., Franx, M., Illingworth, G. D., Marchesini, D., & Quadri, R. F. 2009, *ApJ*, 700, 221
- Lehmer, B. D., Alexander, D. M., Bauer, F. E., Brandt, W. N., Goulding, A. D., Jenkins, L. P., Ptak, A., & Roberts, T. P. 2010, *ApJ*, 724, 559
- Lehmer, B. D. et al. 2012, *ApJ*, 752, 46
- Leitner, S. N. 2012, *ApJ*, 745, 149
- Luo, B. et al. 2008, *ApJS*, 179, 19
- Luo, B. et al. 2010, *ApJS*, 187, 560
- Luo, B. et al. 2011, *ApJ*, 740, 37
- Lusso, E. et al. 2011, *A&A*, 534, 110
- Lyons, L. 1991, *Data Analysis for Physical Science Students* (Cambridge: Cambridge Univ. Press)
- Marchesini, D., Stefanon, M., Brammer, G. B., & Whitaker, K. E. 2012, *ApJ*, 748, 126
- Marconi, A., & Hunt, L. K. 2003, *ApJ*, 589, L21
- Merloni, A. et al. 2010, *ApJ*, 708, 137
- Mineo, S., Gilfanov, M., & Sunyaev, R. 2012, *MNRAS*, 419, 2095
- Mullaney, J. R. et al. 2012, *MNRAS*, 419, 95
- Murphy, K. D., & Yaqoob, T. 2009, *MNRAS*, 397, 1549
- Mushotzky, R. F., Cowie, L. L., Barger, A. J., & Arnaud, K. A. 2000, *Nature*, 404, 459
- Nandra, K. et al. 2007, *ApJ*, 660, L11
- Oke, J. B., & Gunn, J. E. 1983, *ApJ*, 266, 713
- Peng, Y.-j., Lilly, S. J., Kovac, K., et al. 2010, *ApJ*, 721, 193
- Rafferty, D. A., Brandt, W. N., Alexander, D. M., Xue, Y. Q., Bauer, F. E., Lehmer, B. D., Luo, B., & Papovich, C. 2011, *ApJ*, 742, 3
- Ranalli, P., Comastri, A., & Setti, G. 2003, *A&A*, 399, 39
- Reines, A. E., Sivakoff, G. R., Johnson, K. E., & Brogan, C. L. 2011, *Nature*, 470, 66
- Salpeter, E. E. 1955, *ApJ*, 121, 161
- Salvato, M. et al. 2011, *ApJ*, 742, 61
- Shen, Y., & Kelly, B. C. 2010, *ApJ*, 713, 41
- Silverman, J. D. et al. 2009, *ApJ*, 696, 396
- Silverman, J. D. et al. 2010, *ApJS*, 191, 124
- Stark, A. A., Gammie, C. F., Wilson, R. W., Bally, J., Linke, R. A., Heiles, C., & Hurwit, M. 1992, *ApJS*, 79, 77
- Swinyard, B. M., Rieke, G. H., Ressler, M., Glasse, A., Wright, G. S., Ferlet, M., & Wells, M. 2004, *SPIE*, 5487, 785
- Szokoly, G. P. et al. 2004, *ApJS*, 155, 271
- Tozzi, P. et al. 2006, *A&A*, 451, 457
- Treister, E., & Urry, C. M. 2006, *ApJ*, 652, L79
- Trump, J. R. et al. 2011, *ApJ*, 743, 144
- Vasudevan, R. V., Mushotzky, R. F., Winter, L. M., & Fabian, A. C. 2009, *MNRAS*, 399, 1553
- Vasudevan, R. V., Fabian, A. C., Gandhi, P., Winter, L. M., & Mushotzky, R. F. 2010, *MNRAS*, 402, 1081
- Vattakunnel, S. et al. 2012, *MNRAS*, 420, 2190
- Woo, J.-H., Treu, T., Malkan, M. A., & Blandford, R. D. 2008, *ApJ*, 681, 925
- Worsley, M. A. et al. 2005, *MNRAS*, 357, 1281
- Wright, G. S. et al. 2004, *SPIE*, 5487, 653
- Xue, Y. Q. et al. 2010, *ApJ*, 720, 368 (X10)
- Xue, Y. Q. et al. 2011, *ApJS*, 195, 10 (X11)
- Yang, Y., Mushotzky, R. F., Barger, A. J., Cowie, L. L., Sanders, D. B., & Steffen, A. T. 2003, *ApJ*, 585, L85
- Zibetti, S., Charlot, S., & Rix, H.-W. 2009, *MNRAS*, 400, 1181